

# FlowLPS: Langevin-Proximal Sampling for Flow-based Inverse Problem Solvers

Jonghyun Park & Jong Chul Ye  
 Graduate School of AI, KAIST  
 {jhpark99, jong.ye}@kaist.ac.kr



Figure 1. **Qualitative results of FlowLPS.** (a) Motion deblurring, (b) Gaussian deblurring, (c) Super-resolution ( $\times 12$ ) and (d) random inpainting results before and after FlowLPS. (e) and (f) are results for box inpainting.

## Abstract

Deep generative models have become powerful priors for solving inverse problems, and various training-free methods have been developed. However, when applied to latent flow models, existing methods often fail to converge to the posterior mode or suffer from manifold deviation within latent spaces. To mitigate this, here we introduce a novel training-free framework, FlowLPS, that solves inverse problems with pretrained flow models via a Langevin–Proximal Sampling (LPS) strategy. Our method integrates Langevin dynamics for manifold-consistent exploration with proximal optimization for precise mode seeking, achieving a superior balance between reconstruction fidelity and perceptual quality across multiple inverse tasks on FFHQ and DIV2K, outperforming state-of-the-art inverse solvers.

## 1. Introduction

The goal of solving inverse problems is to recover underlying signals  $\mathbf{x}_0$  from noisy measurements  $\mathbf{y}$ . Formally, we aim to estimate the clean image  $\mathbf{x}_0$  from

$$\mathbf{y} = \mathcal{A}(\mathbf{x}_0) + \mathbf{n}, \quad (1)$$

where  $\mathcal{A}$  is the forward measurement operator and  $\mathbf{n}$  denotes additive noise, typically modeled as Gaussian:  $\mathbf{n} \sim \mathcal{N}(0, \sigma_n^2 I)$ . Due to the ill-posed nature of inverse problems, multiple solutions may satisfy Eq. (1). Hence, the objective is to find a meaningful solution using prior information so that it aligns with the true data distribution.

Recently, diffusion models [10, 24] and flow-based models [8, 13, 14] have been explored as powerful priors for inverse problems. One prominent line of approach involves guiding the generative sampling trajectory to conform to the

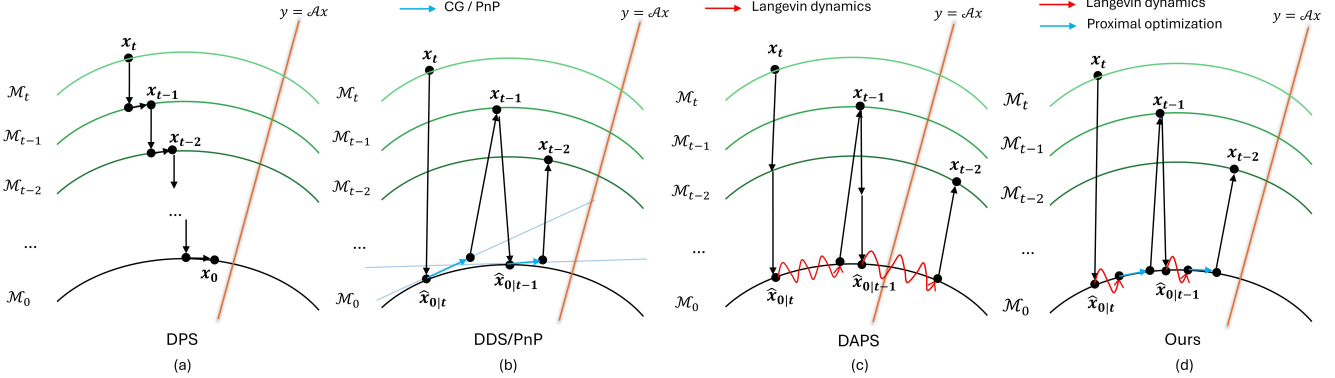


**Figure 2. Comparison of representative inverse problem solvers:** DPS, DDS, DAPS, and the proposed FlowLPS. (a) DPS performs a single gradient-based measurement correction at each timestep, but requires costly backpropagation through the denoising network. (b) DDS and PnP decompose this process into several gradient updates implicitly assuming a locally linear manifold. However, because the data manifold is highly non-linear, these gradient updates often drift off the manifold. (c) DAPS denoises  $\mathbf{x}_t$  using PF-ODE steps and applies iterative Langevin dynamics to approximate the posterior distribution  $p(\mathbf{x}_0|\mathbf{x}_t, \mathbf{y})$ . Such Langevin dynamics ensure posterior consistency but do not guarantee convergence toward the posterior mode. (d) In contrast, FlowLPS first performs a few Langevin dynamics steps to rectify the initial estimate and obtain a manifold-consistent posterior anchor, and then applies proximal optimization to seek the mode of the posterior near this anchor, achieving stable and high-fidelity reconstructions in latent space.

measurements. Methods like MCG [3], DPS [4], and IIGDM [23] aim to approximate the posterior distribution  $p(\mathbf{x}_t|\mathbf{y})$  at each timestep  $t$  through Tweedie formula  $\hat{\mathbf{x}}_{0|t} := \mathbb{E}[\mathbf{x}_0|\mathbf{x}_t]$ . However, Tweedie-guided updates suffer from high variance at early timesteps [25], often degrading reconstruction quality. Variational formulations such as RED-diff [15] attempt to address this via explicit optimization. Another prominent line of work, represented by DAPS [27], employs stochastic Langevin dynamics to approximate the posterior  $p(\mathbf{x}_0|\mathbf{x}_t, \mathbf{y})$  at each timestep. This approach enforces manifold consistency and robust reconstruction by perturbing  $\hat{\mathbf{x}}_{0|t}$  along the posterior distribution.

Despite these advances, applying such ideas in latent space, especially with modern VAE-based models like Stable Diffusion or FLUX, remains challenging. Naively transplanting pixel-space algorithms into latent space often produces blurry outputs, primarily because the VAE decoder introduces significant non-linearity. This transforms the linear measurement operator into a non-linear one with respect to the latent variable and exacerbates the curvature of the data manifold, thereby breaking the local linear manifold assumption [21, 22]. Although recent methods like DDS [5], DAPS, FlowDPS [11], FLAIR [7] and PnP-based solvers such as Flower [20] partially alleviate this through improved measurement consistency through iterative update, they still struggle to maintain both manifold fidelity and mode convergence simultaneously.

In this work, we address this challenge by introducing *FlowLPS* (Langevin–Proximal Sampling for Flow Models), a training-free framework for solving inverse problems with flow-based generative models in the latent space. Our key

idea is a hybrid Langevin–proximal sampling strategy that synergizes sampling-based exploration with optimization-based mode seeking. More specifically, FlowLPS leverages Langevin dynamics for a dual purpose: 1) to rectify the initial estimate by traversing it towards the high-density region of the posterior distribution (manifold correction), and 2) a manifold-consistent reference point (manifold anchoring). Starting from this improved state, we then apply proximal optimization to seek the posterior mode. Because the optimization is anchored to a state that is aligned with the data manifold, our method effectively circumvents the local minima and off-manifold drift issues inherent in pure optimization approaches.

This two-stage design preserves manifold structure while achieving stable and high-fidelity reconstruction. As illustrated in Fig. 2, FlowLPS seamlessly unifies DDS, PnP, and DAPS, providing a better trade-off between manifold fidelity and mode convergence. Furthermore, by integrating a re-noising scheme grounded in the preconditioned Crank–Nicolson (pCN) method [2, 6, 26], our method achieves greater image diversity and higher fidelity while avoiding off-manifold artifacts. Our key contributions are:

- 1. Manifold-aware mode-seeking optimization.** We propose a hybrid strategy that couples Langevin dynamics for manifold correction and anchoring with proximal optimization for mode seeking. This effectively combines the advantages of DAPS and DDS/PnP while mitigating their respective weaknesses.
- 2. Stability mechanisms for latent-space flow models.** We further propose a re-noising scheme inspired by pCN, which interpolates between the predicted and Gaussian

noise, thereby improving convergence stability and image quality during latent-space optimization.

3. **State-of-the-art performance.** Extensive experiments on FFHQ and DIV2K demonstrate that FlowLPS significantly outperforms diffusion- and flow-based baselines for latent-space inverse problems.

## 2. Related Work

Early approaches to solving inverse problems with generative models focus on guiding the sampling trajectory using the posterior score function:

$$\nabla_{\mathbf{x}_t} \log p(\mathbf{x}_t | \mathbf{y}) = \nabla_{\mathbf{x}_t} \log p(\mathbf{x}_t) + \nabla_{\mathbf{x}_t} \log p(\mathbf{y} | \mathbf{x}_t).$$

While the first term is available via the diffusion model’s score, the computation of the likelihood term  $\nabla_{\mathbf{x}_t} \log p(\mathbf{y} | \mathbf{x}_t)$  is generally intractable. DPS [4] approximates the intractable likelihood  $p(\mathbf{y} | \mathbf{x}_t)$  using Tweedie’s formula, leading to  $p(\mathbf{y} | \mathbf{x}_t) \approx p(\mathbf{y} | \hat{\mathbf{x}}_{0|t})$ . PIGDM [23] instead assumes a Gaussian posterior  $p(\mathbf{x}_0 | \mathbf{x}_t) \approx \mathcal{N}(\hat{\mathbf{x}}_{0|t}, r_t^2 I)$  with a tunable hyperparameter  $r_t$ . While effective, these methods require computationally expensive backpropagation at every timestep as shown in Fig. 2(a).

To avoid this cost, subsequent methods such as MPGD [9], FlowChef [17], and PnP-Flow [16] guide the trajectory using the gradient of the measurement loss with respect to the denoised estimate  $\hat{\mathbf{x}}_{0|t}$  (see Fig. 2(b)). However, performing a single gradient update per timestep often provides insufficient measurement consistency [22].

More recent works perform multiple optimization steps at each timestep. For example, DDS [5] introduced multi-step Krylov subspace method to refine measurement consistency while approximately preserving the prior manifold. However, these updates implicitly assume an affine data manifold. In modern latent spaces with non-linear VAE decoders, this assumption no longer holds, i.e. multiple updates from  $\hat{\mathbf{x}}_{0|t}$  can easily push the samples off the data manifold, leading to visual artifacts [21]. Plug-and-Play (PnP) methods such as DiffPIR [29] and Flower [20] extend DDS using Tweedie’s denoising followed by proximal optimization:

$$\mathbf{x}_{0|t}^* = \arg \min_{\mathbf{x}} \|\mathbf{y} - \mathcal{A}(\mathbf{x})\|^2 + \lambda \|\mathbf{x} - \hat{\mathbf{x}}_0\|^2. \quad (2)$$

Unfortunately, PnP approaches face a similar off-manifold issue. Here, the problem lies not in the gradient step but in the optimization anchor: the Tweedie estimate  $\hat{\mathbf{x}}_0$  itself is often off-manifold, especially at early timesteps with high noise. Starting proximal optimization from such points can further exacerbate off-manifold artifacts.

DAPS [27] adopts a different strategy: it applies probability flow ODE steps for denoising, followed by extensive Langevin dynamics to ensure  $\hat{\mathbf{x}}_{0|t} \sim p(\mathbf{x}_0 | \mathbf{x}_t, \mathbf{y})$ . While this maintains manifold consistency, pure Langevin dynamics do not guarantee convergence to the posterior mode and require many iterations (see Fig. 2(c)).

Our method addresses these limitations by synergizing the strengths of both paradigms. Unlike DDS and PnP methods, which suffer from off-manifold drift by directly optimizing uncorrected estimates, and unlike DAPS, which preserves manifold consistency but fails to locate the mode efficiently, FlowLPS strategically utilizes Langevin dynamics to bridge this gap. Crucially, we employ Langevin steps not for full sampling, but to rectify the initial deviation of the Tweedie estimate (Correction) and to establish a valid reference point for optimization (Anchoring). This corrected anchor allows the subsequent proximal step to aggressively seek the posterior mode while preserving high manifold fidelity, as shown in Fig. 2(d). Since our approach relies on Langevin dynamics primarily for initialization and anchoring rather than requiring a fully converged sample, it necessitates far fewer iterations compared to pure sampling methods (as in DAPS). This significantly enhances both stability and efficiency. Moreover, as the reverse flow proceeds and the estimate naturally aligns with the posterior distribution, these intermediate Langevin steps can be gradually reduced to further conserve the computational budget.

## 3. FlowLPS

### 3.1. Flow Matching

Let  $p$  and  $q$  denote the source and target distributions defined over  $\mathbb{R}^d$ . We assume that we can access data samples  $\mathbf{x}_0 \sim q(\mathbf{x}_0)$  but not the distribution  $q$  itself. The goal of flow models is to generate samples from the target distribution  $q$  starting from the source distribution  $p$ . To achieve this, a time-dependent probability path  $p_t$  is constructed such that  $p_1 = p$  and  $p_0 = q$ , via a time-dependent flow, governed by the reverse ODE with the vector field  $\mathbf{v} : [0, 1] \times \mathbb{R}^d \rightarrow \mathbb{R}^d$ :

$$d\mathbf{x}_t = \mathbf{v}_t(\mathbf{x}_t) dt, \quad \mathbf{x}_1 \sim p_1 = p. \quad (3)$$

To estimate the *marginal* vector field  $\mathbf{v}_t$ , we use the parameterized *marginal* velocity field  $\mathbf{v}_t^\theta$  that is estimated using the *conditional flow matching* (CFM) [13]:

$$\mathcal{L}_{CFM} = \mathbb{E}_{t, \mathbf{x}_0 \sim q, \mathbf{x}_t \sim p_t(\mathbf{x}_t | \mathbf{x}_0)} \|\mathbf{v}_t^\theta(\mathbf{x}_t) - \mathbf{v}_t(\mathbf{x}_t | \mathbf{x}_0)\|^2, \quad (4)$$

where  $\mathbf{v}_t(\mathbf{x}_t | \mathbf{x}_0)$  denotes a conditional velocity field. For the case of rectified flow [14],  $\mathbf{x}_t$  can be represented by

$$\mathbf{x}_t = t\mathbf{x}_1 + (1-t)\mathbf{x}_0, \quad (5)$$

where the pair  $(\mathbf{x}_0, \mathbf{x}_1)$  is drawn from the independent coupling  $\pi(\mathbf{x}_0, \mathbf{x}_1) = q(\mathbf{x}_0)p(\mathbf{x}_1)$ . Under this coupling, the corresponding conditional vector field becomes  $\mathbf{v}_t(\mathbf{x}_t | \mathbf{x}_0) = \mathbf{x}_1 - \mathbf{x}_0$ . Then, the corresponding minimizer of Eq. (4) satisfies

$$\mathbf{v}_t^\theta(\mathbf{x}_t) = \mathbb{E}[\mathbf{x}_1 - \mathbf{x}_0 | \mathbf{x}_t] = \mathbb{E}[\mathbf{x}_1 | \mathbf{x}_t] - \mathbb{E}[\mathbf{x}_0 | \mathbf{x}_t]. \quad (6)$$

Accordingly, discretizing the reverse ODE Eq. (3) using Euler's method leads to the following reverse update:

$$\begin{aligned} \mathbf{x}_{t-\Delta t} &= \mathbf{x}_t - \Delta t (\mathbb{E}[\mathbf{x}_1|\mathbf{x}_t] - \mathbb{E}[\mathbf{x}_0|\mathbf{x}_t]) \\ &= (1 - (t - \Delta t))\mathbb{E}[\mathbf{x}_0|\mathbf{x}_t] + (t - \Delta t)\mathbb{E}[\mathbf{x}_1|\mathbf{x}_t], \end{aligned} \quad (7)$$

where we use Eq. (5). This implies that the flow-driven reverse sampling can be equivalently represented by the linear interpolation between the posterior estimate of the clean image  $\mathbb{E}[\mathbf{x}_0|\mathbf{x}_t]$  and the noise  $\mathbb{E}[\mathbf{x}_1|\mathbf{x}_t]$ , which can be represented by

$$\mathbb{E}[\mathbf{x}_0|\mathbf{x}_t] = \mathbf{x}_t - t\mathbf{v}_t(\mathbf{x}_t), \quad \mathbb{E}[\mathbf{x}_1|\mathbf{x}_t] = \mathbf{x}_t + (1 - t)\mathbf{v}_t(\mathbf{x}_t) \quad (8)$$

### 3.2. Langevin-Proximal Posterior Sampling

Given the forward model in Eq. (1), generative inverse solvers aim to find a sample that 1) maximizes the posterior density,  $\log p(\mathbf{x}_0|\mathbf{y})$ , or 2) resides in its most probable region. The first case corresponds to the mode seeking approach, whereas the second approach corresponds to the posterior sampling approach. FlowLPS seek to synergistically integrate the core principles of mode-seeking and Langevin dynamics into a unified framework.

**Langevin dynamics for posterior sampling.** First, we adopt the DAPS approach, which applies multiple Langevin dynamics steps to sample from the joint posterior  $p(\mathbf{x}_0|\mathbf{x}_t, \mathbf{y})$ . Assuming  $p(\mathbf{x}_0|\mathbf{x}_t) = \mathcal{N}(\hat{\mathbf{x}}_{0|t}, s_t^2 I)$  for a given hyperparameter  $s_t$ , we can achieve a closed form expression for  $\nabla_{\mathbf{x}_0} \log p(\mathbf{x}_0|\mathbf{x}_t, \mathbf{y})$  via Bayes' rule:

$$\nabla_{\mathbf{x}_0} \log p(\mathbf{x}_0|\mathbf{x}_t, \mathbf{y}) = \nabla_{\mathbf{x}_0} (\log p(\mathbf{y}|\mathbf{x}_0) + \log p(\mathbf{x}_0|\mathbf{x}_t)). \quad (9)$$

Applying Langevin dynamics to this posterior with step size  $\zeta_t$  yields:

$$\begin{aligned} \hat{\mathbf{x}}_{0|t}^{(k+1)} &= \hat{\mathbf{x}}_{0|t}^{(k)} + \zeta_t \nabla_{\hat{\mathbf{x}}_{0|t}^{(k)}} \log p(\hat{\mathbf{x}}_{0|t}^{(k)}|\mathbf{x}_t, \mathbf{y}) \\ &\quad + \sqrt{2\zeta_t} \epsilon, \quad \epsilon \sim \mathcal{N}(0, I), \end{aligned} \quad (10)$$

Additionally, one can perform Langevin dynamics updates on the noise distribution to obtain more suitable noise samples, which often leads to improved results. The importance of proper noise initialization was also highlighted in previous works, such as FlowDPS and D-Flow [1]. To ensure the noise samples remain within the prior manifold while promoting diversity, we employ the preconditioned Crank–Nicolson (pCN) transition kernel. Formally, for a current noise estimate  $\hat{\mathbf{x}}_{1|t}^{(i)}$ , the pCN update rule targeting the standard normal distribution is given by [2]:

$$\hat{\mathbf{x}}_{1|t}^{(i+1)} = \rho_t \hat{\mathbf{x}}_{1|t}^{(i)} + \sqrt{1 - \rho_t^2} \mathbf{z}, \quad \mathbf{z} \sim \mathcal{N}(0, I), \quad (11)$$

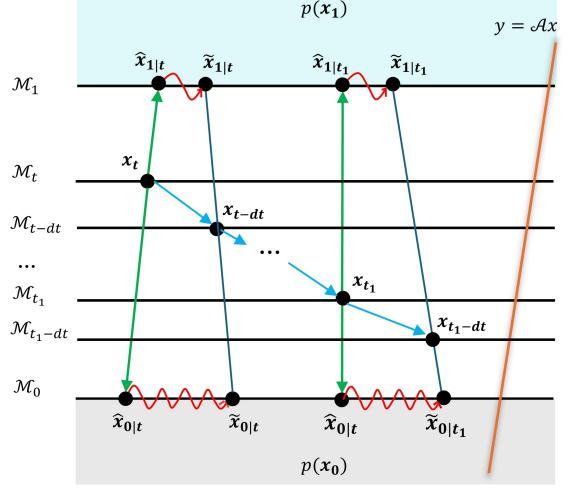


Figure 3. **Manifold-preserving update.** The clean image is iteratively updated using Langevin optimization combined with hybrid noise sampling using pCN, ensuring that the resulting states remain on the data manifold.

where  $\rho_t \in [0, 1]$ . The acceptance probability is always 1 since the target distribution  $p(\mathbf{x}_1)$  is standard normal. In our practical implementation, we initialize the chain with the model's noise estimate  $\hat{\mathbf{x}}_{1|t}^{(0)} = \mathbf{x}_t + (1 - t)\mathbf{v}_t(\mathbf{x}_t)$ . With this initialization, the first step of Eq. (11) with  $\rho_t := \sqrt{1 - (t - \Delta t)}$  becomes equivalent to the hybrid re-noising strategy in FlowDPS, which enhances sample diversity by interpolating between the model-predicted noise and stochastic Gaussian noise.

Analogous to DAPS, Proposition 1 shows that our Langevin and pCN update ensures a manifold-preserving behavior:

**Proposition 1.** *Given the sampling updates defined by Eq. (10) and Eq. (11), their affine combination  $\mathbf{x}_{t'} = (1 - t')\hat{\mathbf{x}}_{0|t}^{(\infty)} + t'\hat{\mathbf{x}}_{1|t}^{(k)}$ ,  $k \geq 1$  follows the distribution*

$$\mathbf{x}_{t'} \sim p(\mathbf{x}_{t'}|\mathbf{y}). \quad (12)$$

This finding is illustrated in Fig. 3, ensuring that the resulting flow update resides in the manifold, thereby guaranteeing stability in the flow ODE.

**Langevin-proximal update.** In designing generative inverse solvers using latent diffusion and flow models, the main challenge is to balance two competing objectives: 1) *manifold consistency*: ensuring estimates lie on the correct manifold, and 2) *measurement fidelity*: minimizing the data fidelity. Existing methods struggle to satisfy both. For instance, DDS and Flower focus on measurement fidelity and suffer from off-manifold drift, while DAPS maintains manifold consistency through Langevin dynamics but fails to converge to the posterior mode.

To address this, we couple proximal optimization with Langevin dynamics, combining their complementary strengths. Their connection is formalized in the following proposition whose proof can be found in Appendix A.

**Proposition 2.** Assume  $p(\mathbf{x}_0|\mathbf{x}_t) = \mathcal{N}(\hat{\mathbf{x}}_{0|t}, s^2 I)$ . Then,

$$\mathbf{x}_{0|t}^* = \arg \max_{\mathbf{x}_0} \log p(\mathbf{x}_0|\mathbf{x}_t, \mathbf{y}). \quad (13)$$

is the solution of the following proximal optimization:

$$\min_{\mathbf{x}_0} \|\mathbf{y} - \mathcal{A}(\mathbf{x}_0)\|^2 + \frac{\sigma_n^2}{s_t^2} \|\mathbf{x}_0 - \hat{\mathbf{x}}_{0|t}\|^2 \quad (14)$$

By Proposition 2, solving the proximal problem in Eq. (2) is equivalent to finding the maximum a posteriori (MAP) estimate of  $p(\mathbf{x}_0|\mathbf{x}_t, \mathbf{y})$ . Building on this insight, FlowLPS introduces a two-phase update at each timestep:

**Phase 1: Manifold-consistent anchoring.** We perform  $N_L$ -step Langevin dynamics updates to align the current estimate with the posterior distribution:

$$\hat{\mathbf{x}}_{0|t}^{(k+1)} = \hat{\mathbf{x}}_{0|t}^{(k)} + \zeta_t \nabla \log p(\hat{\mathbf{x}}_{0|t}^{(k)}|\mathbf{x}_t, \mathbf{y}) + \sqrt{2\zeta_t} \epsilon.$$

This step encourages  $\hat{\mathbf{x}}_{0|t}$  to be aligned with the posterior manifold, promoting manifold consistency.

**Phase 2: Mode-seeking from manifold anchor.** Starting from the manifold-consistent anchor, we perform proximal optimization:

$$\mathbf{x}_{0|t}^* = \arg \min_{\mathbf{x}} \|\mathbf{y} - \mathcal{A}(\mathbf{x}_0)\|^2 + \frac{\sigma_n^2}{s_t^2} \|\mathbf{x}_0 - \hat{\mathbf{x}}_{0|t}^{(N_L)}\|^2$$

Here, the regularization term anchors the optimization near the manifold while allowing the solution to converge toward the posterior mode. This synergy between exploration (Langevin) and convergence (proximal) yields high-fidelity, perceptually sharp reconstructions.

**Hyperparameter selection.** The parameter  $s_t$  in the proximal objective balances the trade-off between the data fidelity term and the regularization term anchored at  $\hat{\mathbf{x}}_{0|t}^{(N_L)}$ . Inspired by the blending rationale in FlowDPS [11], which highlights the importance of early measurement consistency, we set  $s_t^2 = t$ .

For the noise refinement defined in Eq. (11), we determine the number of steps empirically. We observed that applying multiple pCN steps tends to excessively perturb the estimate, diluting the valuable structural information embedded in the model's prediction. This leads to over-smoothed reconstructions by weakening the structural correlation with  $\mathbf{x}_t$  (see Appendix C.2). Consequently, we adopt a single pCN step as the optimal choice. Combined with an adaptive mixing rate  $\rho_t = \sqrt{1 - \sigma_t}$ , this strategy injects sufficient stochasticity to escape local minima while preserving the deterministic guidance of the flow trajectory (see Sec. 4.3.2).

The complete algorithm is summarized in Algorithm 1 as a latent variable  $\mathbf{z}_t$  update.

---

### Algorithm 1 Algorithm of FlowLPS

---

**Require:**  $\mathbf{y}, \mathcal{A}$ , VAE decoder  $\mathcal{D}$ , flow-based model  $\mathbf{v}_t^\theta$ , Langevin dynamics steps  $N_L$

- 1:  $\mathbf{z}_1 \sim \mathcal{N}(0, I)$
- 2: **for**  $t : 1 \rightarrow 0$  **do**
- 3:      $\mathbf{v}_t \leftarrow \mathbf{v}_t^\theta(\mathbf{z}_t)$
- 4:      $\hat{\mathbf{z}}_{0|t}^{(0)} \leftarrow \mathbf{z}_t - t\mathbf{v}_t$ ,  $\hat{\mathbf{z}}_{1|t} \leftarrow \mathbf{z}_t + (1-t)\mathbf{v}_t$
- 5:      $\hat{\epsilon}_{1|t} \leftarrow \sqrt{1 - (t - \Delta t)} \hat{\mathbf{z}}_{1|t} + \sqrt{t - \Delta t} \epsilon$ ,  $\epsilon \sim \mathcal{N}(0, I)$  ▷ pCN update
- 6:
- 7:     **for**  $j = 0, 1, \dots, N_L - 1$  **do**
- 8:          $Z_j \sim \mathcal{N}(0, I)$
- 9:          $\hat{\mathbf{z}}_{0|t}^{(j+1)} \leftarrow \hat{\mathbf{z}}_{0|t}^{(j)} + \zeta_t \nabla_{\hat{\mathbf{z}}_{0|t}^{(j)}} \log p(\hat{\mathbf{z}}_{0|t}^{(j)}|\mathbf{z}_t, \mathbf{y}) + \sqrt{2\zeta_t} Z_j$  ▷ Langevin dynamics
- 10:     **end for**
- 11:      $\mathbf{z} \leftarrow \hat{\mathbf{z}}_{0|t}^{(N_L)}$
- 12:      $\mathbf{z}_{0|t}^* \leftarrow \operatorname{argmin}_{\mathbf{z}} \|\mathbf{y} - \mathcal{A}(\mathcal{D}(\mathbf{z}))\|^2 + \frac{\sigma_n^2}{t} \|\mathbf{z} - \hat{\mathbf{z}}_{0|t}^{(N_L)}\|^2$  ▷ Proximal optimization
- 13:
- 14:      $\mathbf{z}_{t-\Delta t} \leftarrow (1 - (t - \Delta t)) \mathbf{z}_{0|t}^* + (t - \Delta t) \hat{\epsilon}_{1|t}$
- 15: **end for**
- 16: **return**  $\mathcal{D}(\mathbf{z}_{0|t}^*)$

---

## 4. Experimental Results

### 4.1. Experimental Setup

**Datasets and Evaluation Metrics.** We conducted comprehensive evaluations of our model across multiple inverse problems using high-resolution images from two distinct datasets: 1k images from the FFHQ dataset and 0.8k images from the DIV2K dataset. All experiments were performed at  $768 \times 768$  resolution by resizing the original images. Our evaluation employs dual assessment: PSNR and SSIM for quantifying pixel-level reconstruction fidelity, complemented by FID and LPIPS for measuring perceptual quality and naturalness of generated outputs.

**Baselines.** We benchmark our method against two diffusion-based solvers: RLSD [30] and DAPS [27], the current state-of-the-art diffusion-based solver, and four flow-based solvers: FlowChef [17], FlowDPS [11], FLAIR [7] (the current state-of-the-art flow-based solver), and Flower [20] (concurrent work using PnP-HQS with pure optimization). All diffusion-based methods utilize Stable Diffusion 2 [18] as their backbone, while flow-based methods leverage Stable Diffusion 3 [19]. To ensure fair comparison, diffusion models and flow models operate with the same number of function evaluations (NFEs) respectively. Additional implementation details are provided in Appendix.

**Task Setting.** We used the text prompt "a high quality photo of a face" for the FFHQ dataset and image descriptions generated by DAPE for DIV2K. For all cases, we set the CFG scale to 2.0. We evaluated all methods on five linear tasks: Gaussian deblurring with kernel size 181 and intensity 9.0, Motion deblurring with kernel size 183 and intensity 0.5,

Table 1. Quantitative Results on FFHQ 1k and DIV2K 0.8k datasets with  $\sigma_n = 0.03$ . **Bold**: best. Underline: second best.

Task	Type	Method	FFHQ 1k				DIV2K 0.8k			
			PSNR ( $\uparrow$ )	SSIM ( $\uparrow$ )	FID ( $\downarrow$ )	LPIPS ( $\downarrow$ )	PSNR ( $\uparrow$ )	SSIM ( $\uparrow$ )	FID ( $\downarrow$ )	LPIPS ( $\downarrow$ )
Inpainting (Box)	Diffusion	DAPS	19.77	0.846	53.22	0.139	22.50	0.807	30.57	0.091
		RLSD	13.08	0.766	151.5	0.261	17.11	0.822	75.41	0.148
	Flow	FlowDPS	18.81	0.771	58.49	0.204	21.36	0.756	36.13	0.142
		FlowChef	17.72	0.701	74.07	0.265	21.02	0.688	59.44	0.160
		FLAIR	<b>21.84</b>	0.836	<u>22.63</u>	0.122	<u>23.90</u>	<u>0.845</u>	<u>20.76</u>	<u>0.076</u>
		Flower	21.63	<b>0.876</b>	48.91	<u>0.119</u>	<b>24.41</b>	<b>0.868</b>	22.38	0.081
		Ours	<u>21.68</u>	<u>0.849</u>	<b>21.90</b>	<b>0.107</b>	23.73	0.862	<b>15.50</b>	<b>0.065</b>
Inpainting (Random)	Diffusion	DAPS	30.99	<u>0.884</u>	16.477	<u>0.035</u>	25.53	<u>0.764</u>	<u>24.17</u>	0.064
		RLSD	17.24	0.383	116.6	0.405	16.98	0.396	107.0	0.382
	Flow	FlowDPS	30.36	0.808	32.03	0.109	25.44	0.713	27.96	0.114
		FlowChef	<u>32.07</u>	0.849	63.23	0.077	25.35	0.688	<u>57.82</u>	0.139
		FLAIR	14.09	0.502	131.9	0.443	13.78	0.355	116.9	0.408
		Flower	31.37	0.826	<u>15.76</u>	0.048	<u>28.81</u>	<b>0.843</b>	<u>9.824</u>	<u>0.026</u>
		Ours	<b>34.34</b>	<b>0.886</b>	<b>7.460</b>	<b>0.019</b>	<b>28.85</b>	<u>0.841</u>	<u>9.360</u>	<u>0.025</u>
Gaussian Deblurring	Diffusion	DAPS	<u>28.20</u>	<u>0.772</u>	49.83	0.174	<u>21.94</u>	<b>0.550</b>	75.34	0.286
		RLSD	25.50	0.674	88.23	0.227	21.86	0.538	104.1	<b>0.242</b>
	Flow	FlowDPS	26.87	0.715	45.19	0.201	21.17	0.519	78.79	0.322
		FlowChef	24.87	0.690	46.61	0.260	21.19	0.542	102.6	0.363
		FLAIR	26.84	0.704	<b>29.03</b>	<u>0.165</u>	21.27	0.509	<u>63.97</u>	<u>0.276</u>
		Flower	<b>28.67</b>	<b>0.796</b>	94.34	0.167	21.84	0.561	88.65	0.312
		Ours	27.76	0.737	<u>31.22</u>	<b>0.130</b>	<b>21.97</b>	<u>0.549</u>	<b>63.62</b>	<b>0.242</b>
Motion Deblurring	Diffusion	DAPS	<u>30.85</u>	<u>0.830</u>	43.17	0.095	<b>24.56</b>	<b>0.661</b>	49.03	0.136
		RLSD	25.73	0.719	92.52	0.269	22.16	0.578	87.06	0.260
	Flow	FlowDPS	25.98	0.704	48.88	0.229	20.91	0.514	81.88	0.325
		FlowChef	20.52	0.626	69.13	0.388	19.84	0.528	128.0	0.431
		FLAIR	28.50	0.744	<u>22.62</u>	0.113	22.95	0.579	<u>43.70</u>	<u>0.174</u>
		Flower	<b>31.00</b>	<b>0.834</b>	67.56	<u>0.087</u>	23.51	0.624	68.60	0.207
		Ours	29.81	0.774	<b>21.15</b>	<b>0.067</b>	<u>24.29</u>	<u>0.642</u>	<b>36.02</b>	<b>0.110</b>
Super-Resolution (x12)	Diffusion	DAPS	<u>27.61</u>	0.727	41.55	0.177	18.02	0.415	80.84	0.368
		RLSD	22.18	0.644	133.5	0.404	18.81	0.450	187.3	0.430
	Flow	FlowDPS	26.68	0.725	36.07	<u>0.171</u>	21.77	0.543	<u>67.01</u>	<u>0.272</u>
		FlowChef	26.59	0.721	58.39	0.208	<u>21.86</u>	<u>0.563</u>	96.32	0.305
		FLAIR	26.82	<u>0.739</u>	<b>31.33</b>	0.181	20.42	0.475	67.91	0.285
		Flower	<b>28.10</b>	<b>0.769</b>	49.55	0.179	<b>22.16</b>	<b>0.567</b>	75.64	0.280
		Ours	27.12	0.716	<u>34.54</u>	<b>0.158</b>	21.16	0.505	<b>65.52</b>	<b>0.267</b>

Super-resolution with bicubic interpolation at 12x scaling factor, Box Inpainting with a  $384 \times 384$  rectangular mask for FFHQ and two  $192 \times 192$  rectangular masks for DIV2K, and Random Inpainting masking 70% of the image. To simulate realistic conditions, all measurement operators incorporate additional Gaussian noise with  $\sigma_n = 0.03$ .

## 4.2. Results

Table 1 summarizes the quantitative comparison across all tasks and datasets. The results highlight a clear distinction in performance characteristics among methods, which we analyze through the lens of the perception-distortion trade-off [12, 28]. Existing solvers exhibit polarized performance limitations: 1) Distortion-centric methods: Methods relying on proximal optimization (Flower), gradient guidance (FlowDPS), or pure sampling (DAPS) tend to minimize pixel-level error (MSE) at the cost of texture details. As shown in Table 1, they achieve reasonable PSNR but suffer from high FID. Qualitatively (Fig. 4), this manifests as over-smoothed and blurry reconstructions. Specifically,

Flower, which relies on pure proximal optimization, often gets trapped in off-manifold local minima due to inaccurate Tweedie initialization, particularly at early timesteps with high noise levels, minimizing MSE without recovering high-frequency details. Similarly, DAPS, despite its Langevin dynamics, fails to converge to the sharp posterior mode, yielding average-like estimates that lack perceptual realism. 2) Perception-centric method (FLAIR): While FLAIR achieves competitive FID scores, it suffers from low PSNR. This indicates a tendency towards hallucination, where the model generates realistic textures that deviate significantly from the ground truth structures (additional visual comparisons are provided in Appendix D.1). 3) Other baselines (RLSD, FlowChef): These methods exhibit suboptimal convergence in high-dimensional latent spaces, resulting in poor scores across both fidelity and perceptual metrics due to noisy or unstable reconstructions.

FlowLPS effectively breaks this trade-off. By utilizing Langevin dynamics for manifold correction followed by proximal optimization for anchored mode seeking, our

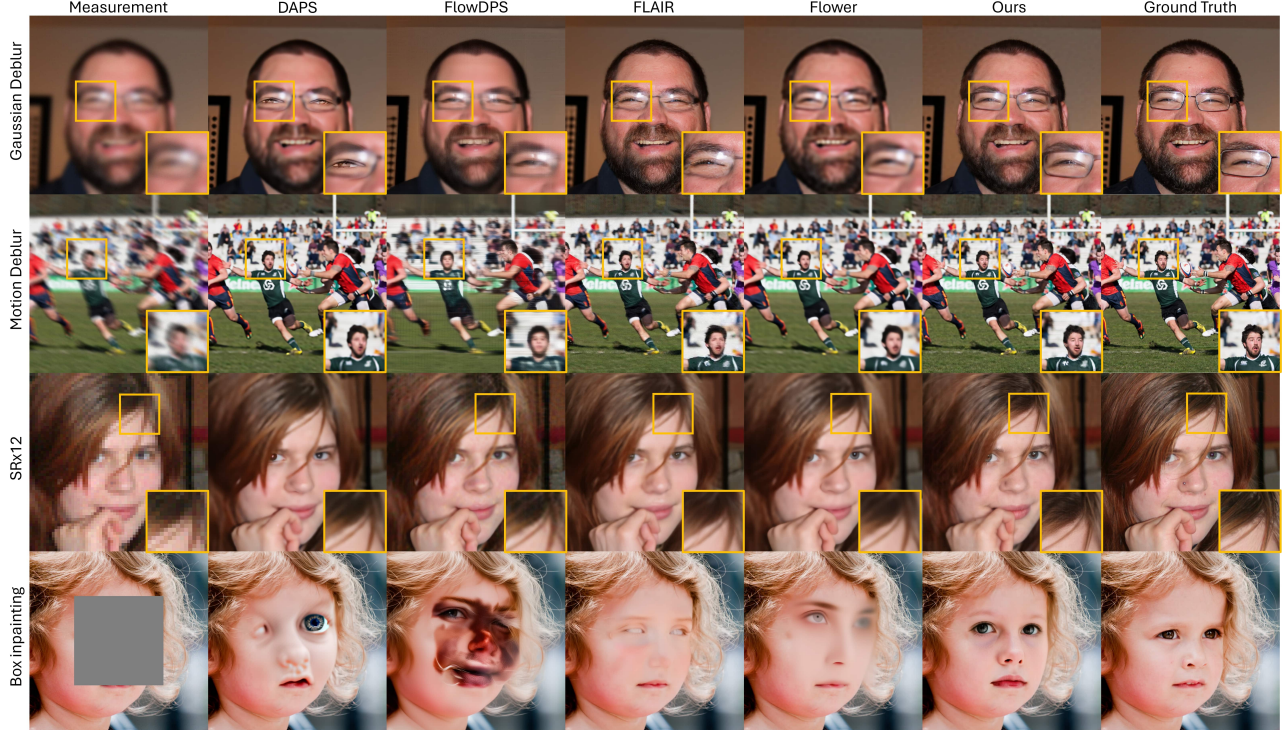


Figure 4. Qualitative comparison on FFHQ and DIV2K datasets.

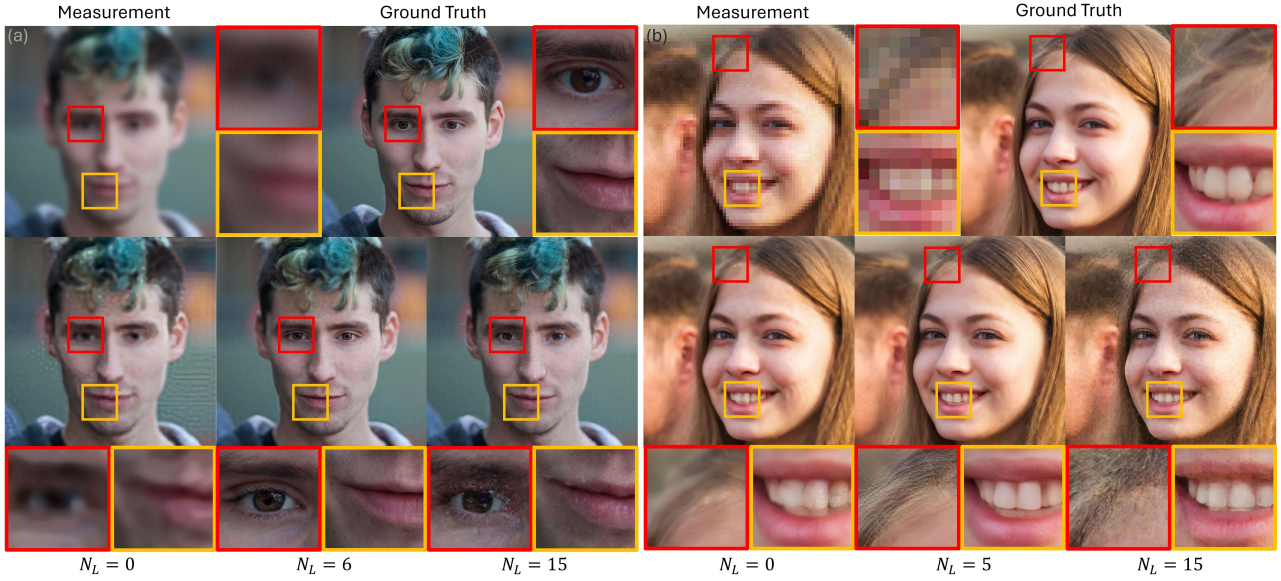


Figure 5. Effect of the number of Langevin steps ( $N_L$ ). (a) Gaussian deblurring and (b) Super-resolution ( $\times 12$ ). Using no Langevin steps ( $N_L = 0$ ) leads to overly smooth and blurry reconstructions due to optimization getting stuck in poor local minima. Excessive Langevin updates ( $N_L = 15$ ) introduce instability and high-frequency noise. Moderate Langevin steps  $N_L = 5 - 7$  achieves an optimal balance, producing detailed restorations while maintaining measurement consistency.

method achieves a superior balance. FlowLPS consistently achieves superior performance across both pixel-level fidelity and perceptual quality metrics. Qualitative results in

Fig. 4 confirm that FlowLPS reconstructs sharp, natural textures (low LPIPS) while maintaining structural faithfulness, outperforming baselines that sacrifice one for the other.

### 4.3. Ablation Studies

#### 4.3.1. Number of Langevin Dynamics Steps( $N_L$ )

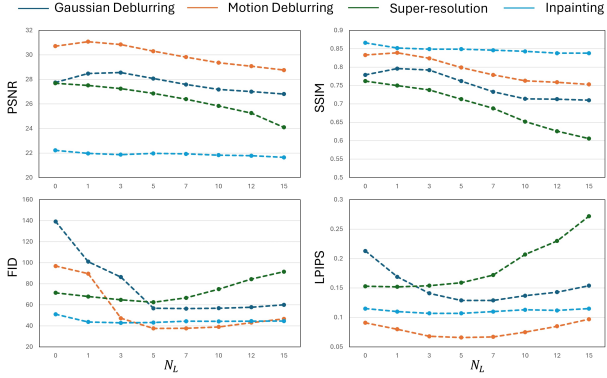


Figure 6. **Quantitative impact of Langevin dynamics steps ( $N_L$ ).** While pixel-level metrics decline with increasing  $N_L$ , perceptual metrics improve until  $N_L \approx 5 - 7$ . This sweet spot balances fidelity and perceptual quality. Excessive stochasticity ( $N_L > 10$ ) degrades all metrics.

We experimented with varying the number of Langevin steps  $N_L$  on 200 FFHQ images. We first set the total Langevin-proximal optimization step  $N_P = 15$ . Fig. 6 illustrates the trade-off: (1) When  $N_L = 0$  (Pure optimization, similar to Flower/DDS), the method degenerates into pure optimization, producing over-smoothed results with high FID/LPIPS due to off-manifold updates. (2) Introducing moderate stochasticity ( $N_L = 5 - 7$ ) significantly improves both pixel-level and perceptual metrics, as Langevin dynamics guide the estimate toward the posterior  $p(\mathbf{x}_0|\mathbf{x}_t, \mathbf{y})$  and provide a manifold-consistent anchor. (3) Excessive stochasticity ( $N_L > 10$ , similar to DAPS) destabilizes convergence and degrades reconstruction fidelity. These results confirm that the proposed hybridization achieves the optimal balance between exploration and exploitation. The improvement from  $N_L = 0$  to  $N_L = 5 - 7$  empirically validates our core claim that Langevin-proximal optimization is superior to pure optimization for latent space flow models. Fig. 5 demonstrates the qualitative impact of this hybrid approach. Additional qualitative results are provided in Appendix C.1.

#### 4.3.2. Impact of Re-noising Strategy ( $\rho_t$ ).

We investigated various schedules for  $\rho_t$ , comparing constant values  $\{0, 0.5\}$  against adaptive schedules  $\{1 - \sigma_t, \sqrt{1 - \sigma_t}\}$ . As shown in Table 2, adaptive schedules significantly outperform fixed ones. Specifically,  $\rho_t = \sqrt{1 - \sigma_t}$  yields the most natural textures (lowest FID and LPIPS). For instance, in Fig. 7,  $\rho_t = \sqrt{1 - \sigma_t}$  successfully reconstructs continuous hair strands across the mask, whereas other schedules fail. This confirms that injecting noise proportional to the remaining uncertainty is key to balancing stochasticity and structural preservation. Furthermore, regarding the pCN update,

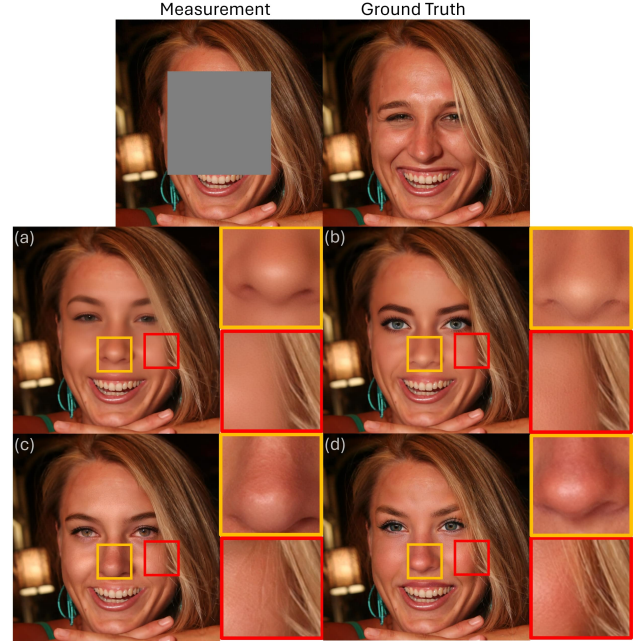


Figure 7. **Qualitative comparison of  $\rho_t$ .** (a)  $\rho_t = 0$ , (b)  $\rho_t = 0.5$ , (c)  $\rho_t = 1 - \sigma_t$ , (d)  $\rho_t = \sqrt{1 - \sigma_t}$ . Our adaptive schedule (d) best preserves high-frequency details and semantic continuity (e.g., hair strands) compared to other schedules.

we found that a single step is optimal. Excessive steps tend to dilute the structural information embedded in the flow model’s prediction, leading to over-smoothing. Detailed comparisons on pCN steps are provided in Appendix C.2.

Table 2. **Comparison of re-noising schedules  $\rho_t$  on FFHQ 0.2k.**

$\rho_t$	PSNR ( $\uparrow$ )	SSIM ( $\uparrow$ )	FID ( $\downarrow$ )	LPIPS ( $\downarrow$ )
0	<b>22.29</b>	0.843	54.21	0.116
0.5	21.47	0.844	53.79	0.111
$1 - \sigma_t$	21.79	0.842	43.56	0.108
$\sqrt{1 - \sigma_t}$	21.94	<b>0.846</b>	<b>42.15</b>	<b>0.106</b>

#### 4.3.3. Dynamic Computational Budget Allocation

We explored the potential of reducing the computational cost by gradually decreasing the number of Langevin steps  $N_L$  during reverse sampling. As detailed in Appendix C.3, linearly reducing  $N_L$  (resulting in a total budget of  $N_P = 10$ ) maintained performance parity. This validates our hypothesis that Langevin dynamics are crucial for manifold correction and anchoring in the early stages but can be safely reduced in later stages.

Separately, we examined the impact of the total proximal budget  $N_P$  (Appendix C.3). Increasing  $N_P$  improves measurement consistency up to about 10 steps, beyond which the benefit diminishes, suggesting that FlowLPS is efficient and does not require extensive iterations for stable convergence.

## 5. Conclusion

We introduced FlowLPS, a training-free framework for solving inverse problems with latent-space flow models through a hybrid Langevin–Proximal optimization strategy. By combining stochastic Langevin dynamics for posterior exploration with proximal updates for precise mode convergence, FlowLPS effectively overcomes the local-minima and off-manifold limitations of prior PnP-HQS approaches such as Flower. Extensive experiments across diverse tasks demonstrate that our method achieves an optimal trade-off between reconstruction fidelity and perceptual realism, outperforming both optimization- and diffusion-based baselines. FlowLPS offers a new perspective that bridges posterior sampling and optimization, providing a principled and efficient route toward robust training-free inference with pretrained flow models.

## References

[1] Heli Ben-Hamu, Omri Puny, Itai Gat, Brian Karrer, Uriel Singer, and Yaron Lipman. D-flow: Differentiating through flows for controlled generation. In *International conference on machine learning*, 2024. 4

[2] Alexandros Beskos, Mark Girolami, Shiwei Lan, Patrick E Farrell, and Andrew M Stuart. Geometric MCMC for infinite-dimensional inverse problems. *Journal of Computational Physics*, 335:327–351, 2017. 2, 4

[3] Hyungjin Chung, Byeongsu Sim, Dohoon Ryu, and Jong Chul Ye. Improving diffusion models for inverse problems using manifold constraints. In *Advances in Neural Information Processing Systems*, 2022. 2

[4] Hyungjin Chung, Jeongsol Kim, Michael Thompson Mccann, Marc Louis Klasky, and Jong Chul Ye. Diffusion posterior sampling for general noisy inverse problems. In *International Conference on Learning Representations*, 2023. 2, 3, 11

[5] Hyungjin Chung, Suhyeon Lee, and Jong Chul Ye. Decomposed diffusion sampler for accelerating large-scale inverse problems. In *The Twelfth International Conference on Learning Representations*, 2024. 2, 3

[6] Simon L Cotter, Gareth O Roberts, Andrew M Stuart, and David White. MCMC methods for functions: modifying old algorithms to make them faster. *Statistical Science*, pages 424–446, 2013. 2

[7] Julius Erbach, Dominik Narnhofer, Andreas Dombos, Bernt Schiele, Jan Eric Lenssen, and Konrad Schindler. Solving inverse problems with flair. In *Advances in Neural Information Processing Systems*, 2025. 2, 5, 11, 12, 15

[8] Patrick Esser, Sumith Kulal, Andreas Blattmann, Rahim Entezari, Jonas Müller, Harry Saini, Yam Levi, Dominik Lorenz, Axel Sauer, Frederic Boesel, et al. Scaling rectified flow transformers for high-resolution image synthesis. In *Forty-first International Conference on Machine Learning*, 2024. 1, 11

[9] Yutong He, Naoki Murata, Chieh-Hsin Lai, Yuhta Takida, Toshimitsu Uesaka, Dongjun Kim, Wei-Hsiang Liao, Yuki Mitsufuji, J Zico Kolter, Ruslan Salakhutdinov, and Stefano Ermon. Manifold preserving guided diffusion. In *The Twelfth International Conference on Learning Representations*, 2024. 3

[10] Jonathan Ho, Ajay Jain, and Pieter Abbeel. Denoising diffusion probabilistic models. *Advances in Neural Information Processing Systems*, 33:6840–6851, 2020. 1

[11] Jeongsol Kim, Bryan Sangwoo Kim, and Jong Chul Ye. Flowdps: Flow-driven posterior sampling for inverse problems. In *Proceedings of the IEEE/CVF international conference on computer vision*, 2025. 2, 5, 11, 12

[12] Christian Ledig, Lucas Theis, Ferenc Husz’ar, Jose Caballero, Andrew Cunningham, Alejandro Acosta, Andrew Aitken, Alykhan Tejani, Johannes Totz, Zehan Wang, et al. Photo-realistic single image super-resolution using a generative adversarial network. In *Proceedings of the IEEE conference on computer vision and pattern recognition*, pages 4681–4690, 2017. 6

[13] Yaron Lipman, Ricky T. Q. Chen, Heli Ben-Hamu, Maximilian Nickel, and Matthew Le. Flow matching for generative modeling. In *The Eleventh International Conference on Learning Representations*, 2023. 1, 3

[14] Xingchao Liu, Chengyue Gong, and qiang liu. Flow straight and fast: Learning to generate and transfer data with rectified flow. In *The Eleventh International Conference on Learning Representations*, 2023. 1, 3, 11

[15] Morteza Mardani, Jiaming Song, Jan Kautz, and Arash Vahdat. A variational perspective on solving inverse problems with diffusion models. *arXiv preprint arXiv:2305.04391*, 2023. 2

[16] Ségolène Tiffany Martin, Anne Gagneux, Paul Hagemann, and Gabriele Steidl. Pnp-flow: Plug-and-play image restoration with flow matching. In *The Thirteenth International Conference on Learning Representations*, 2025. 3

[17] Maitreya Patel, Song Wen, Dimitris N Metaxas, and Yezhou Yang. Steering rectified flow models in the vector field for controlled image generation. *arXiv preprint arXiv:2412.00100*, 2024. 3, 5, 12

[18] Suraj Patil, Pedro Cuenca, Nathan Lambert, and Patrick von Platen. Stable diffusion with diffusers. *Hugging Face Blog*, 2022. [https://huggingface.co/blog/stable\\_diffusion](https://huggingface.co/blog/stable_diffusion). 5, 11

[19] William Peebles and Saining Xie. Scalable diffusion models with transformers. In *Proceedings of the IEEE/CVF International Conference on Computer Vision*, pages 4195–4205, 2023. 5

[20] Mehrsa Pourya, Bassam El Rawas, and Michael Unser. Flower: A flow-matching solver for inverse problems, 2025. 2, 3, 5, 12

[21] Litu Rout, Negin Raoof, Giannis Daras, Constantine Caramanis, Alex Dimakis, and Sanjay Shakkottai. Solving linear inverse problems provably via posterior sampling with latent diffusion models. *Advances in Neural Information Processing Systems*, 36, 2024. 2, 3

[22] Bowen Song, Soo Min Kwon, Zecheng Zhang, Xinyu Hu, Qing Qu, and Liyue Shen. Solving inverse problems with latent diffusion models via hard data consistency. In *The Twelfth International Conference on Learning Representations*, 2024. 2, 3

[23] Jiaming Song, Arash Vahdat, Morteza Mardani, and Jan Kautz. Pseudoinverse-guided diffusion models for inverse

problems. In *International Conference on Learning Representations*, 2023. 2, 3

[24] Yang Song, Jascha Sohl-Dickstein, Diederik P. Kingma, Abhishek Kumar, Stefano Ermon, and Ben Poole. Score-based generative modeling through stochastic differential equations. In *9th International Conference on Learning Representations, ICLR*, 2021. 1

[25] Lingxiao Yang, Shutong Ding, Yifan Cai, Jingyi Yu, Jingya Wang, and Ye Shi. Guidance with spherical gaussian constraint for conditional diffusion. *arXiv preprint arXiv:2402.03201*, 2024. 2

[26] Taehoon Yoon, Yunhong Min, Kyeongmin Yeo, and Minhyuk Sung. Psi-sampler: Initial particle sampling for smc-based inference-time reward alignment in score models. 2025. 2

[27] Bingliang Zhang, Wenda Chu, Julius Berner, Chenlin Meng, Anima Anandkumar, and Yang Song. Improving diffusion inverse problem solving with decoupled noise annealing. *arXiv preprint arXiv:2407.01521*, 2024. 2, 3, 5, 12

[28] Richard Zhang, Phillip Isola, Alexei A Efros, Eli Shechtman, and Oliver Wang. The unreasonable effectiveness of deep features as a perceptual metric. In *Proceedings of the IEEE conference on computer vision and pattern recognition*, pages 586–595, 2018. 6

[29] Yuanzhi Zhu, Kai Zhang, Jingyun Liang, Jiezhang Cao, Bihan Wen, Radu Timofte, and Luc Van Gool. Denoising diffusion models for plug-and-play image restoration. In *Proceedings of the IEEE/CVF Conference on Computer Vision and Pattern Recognition*, pages 1219–1229, 2023. 3

[30] Nicolas Zilberstein, Morteza Mardani, and Santiago Segarra. Repulsive latent score distillation for solving inverse problems. In *International Conference on Learning Representations*, 2024. 5, 12

## A. Proofs

**Proposition 1.** Given the sampling updates defined by Eq. (10) and Eq. (11), their affine combination  $\mathbf{x}_{t'} = (1 - t')\hat{\mathbf{x}}_{0|t}^{(\infty)} + t'\hat{\mathbf{x}}_{1|t}^{(k)}$ ,  $k \geq 1$  follows the distribution

$$\mathbf{x}_{t'} \sim p(\mathbf{x}_{t'} | \mathbf{y}). \quad (12)$$

*Proof.* Recall that the rectified flow framework is formulated under the independent coupling  $\pi(\mathbf{x}_0, \mathbf{x}_1) = q(\mathbf{x}_0)p(\mathbf{x}_1)$  [14]. Since the measurement  $\mathbf{y}$  depends only on the clean signal  $\mathbf{x}_0$ , the joint posterior factorizes as:

$$\begin{aligned} p(\mathbf{x}_0, \mathbf{x}_1 | \mathbf{y}) &= \frac{p(\mathbf{y} | \mathbf{x}_0, \mathbf{x}_1)p(\mathbf{x}_0, \mathbf{x}_1)}{p(\mathbf{y})} \\ &= \frac{p(\mathbf{y} | \mathbf{x}_0)p(\mathbf{x}_0)}{p(\mathbf{y})}p(\mathbf{x}_1) \\ &= p(\mathbf{x}_0 | \mathbf{y})p(\mathbf{x}_1). \end{aligned} \quad (15)$$

Now, assume by inductive hypothesis that the current state follows the marginal distribution  $\mathbf{x}_t \sim p(\mathbf{x}_t | \mathbf{y})$ . By the law of total probability,

$$p(\mathbf{x}_0 | \mathbf{y}) = \int p(\mathbf{x}_0 | \mathbf{x}_t, \mathbf{y})p(\mathbf{x}_t | \mathbf{y})d\mathbf{x}_t. \quad (16)$$

Since the Langevin dynamics step draws  $\hat{\mathbf{x}}_{0|t}^{(\infty)}$  from the conditional distribution  $p(\mathbf{x}_0 | \mathbf{x}_t, \mathbf{y})$  given  $\mathbf{x}_t$ , the estimate marginally follows  $\hat{\mathbf{x}}_{0|t}^{(\infty)} \sim p(\mathbf{x}_0 | \mathbf{y})$ .

Simultaneously, the pCN update leaves the prior invariant, yielding  $\hat{\mathbf{x}}_{1|t}^{(k)} \sim p(\mathbf{x}_1)$  for  $k \geq 1$ . Thus, the pair  $(\hat{\mathbf{x}}_{0|t}^{(\infty)}, \hat{\mathbf{x}}_{1|t}^{(1)}) \sim p(\mathbf{x}_0 | \mathbf{y})p(\mathbf{x}_1)$ .

Therefore, their affine combination  $\mathbf{x}_{t'} = (1 - t')\hat{\mathbf{x}}_{0|t}^{(\infty)} + t'\hat{\mathbf{x}}_{1|t}^{(k)}$  is a valid sample from the target marginal distribution  $p(\mathbf{x}_{t'} | \mathbf{y})$ .  $\square$

**Proposition 2.** Assume  $p(\mathbf{x}_0 | \mathbf{x}_t) = \mathcal{N}(\hat{\mathbf{x}}_{0|t}, s_t^2 I)$ . Then,

$$\mathbf{x}_{0|t}^* = \arg \max_{\mathbf{x}_0} \log p(\mathbf{x}_0 | \mathbf{x}_t, \mathbf{y}). \quad (13)$$

is the solution of the following proximal optimization:

$$\min_{\mathbf{x}_0} \|\mathbf{y} - \mathcal{A}(\mathbf{x}_0)\|^2 + \frac{\sigma_n^2}{s_t^2} \|\mathbf{x}_0 - \hat{\mathbf{x}}_{0|t}\|^2 \quad (14)$$

*Proof.* By Bayes' rule and the Markov property,

$$\begin{aligned} p(\mathbf{y} | \mathbf{x}_0, \mathbf{x}_t) &= p(\mathbf{y} | \mathbf{x}_0), \\ p(\mathbf{x}_0 | \mathbf{x}_t, \mathbf{y}) &= \frac{p(\mathbf{y} | \mathbf{x}_0, \mathbf{x}_t)p(\mathbf{x}_0 | \mathbf{x}_t)}{p(\mathbf{y} | \mathbf{x}_t)} \\ &\propto p(\mathbf{y} | \mathbf{x}_0)p(\mathbf{x}_0 | \mathbf{x}_t). \end{aligned}$$

Substituting the Gaussian forms gives

$$\begin{aligned} \max_{\mathbf{x}_0} \log p(\mathbf{x}_0 | \mathbf{x}_t, \mathbf{y}) &= \max_{\mathbf{x}_0} \log p(\mathbf{y} | \mathbf{x}_0) + \log p(\mathbf{x}_0 | \mathbf{x}_t) \\ &= \max_{\mathbf{x}_0} -\frac{\|\mathbf{y} - \mathcal{A}(\mathbf{x}_0)\|^2}{2\sigma_n^2} - \frac{\|\mathbf{x}_0 - \hat{\mathbf{x}}_{0|t}\|^2}{2s_t^2} \\ &= \min_{\mathbf{x}_0} \|\mathbf{y} - \mathcal{A}(\mathbf{x}_0)\|^2 + \frac{\sigma_n^2}{s_t^2} \|\mathbf{x}_0 - \hat{\mathbf{x}}_{0|t}\|^2 \end{aligned}$$

$\square$

## B. Implementation Details

In this section, we provide comprehensive implementation details for FlowLPS and the baseline methods. We utilize Stable Diffusion 2.1 [18] as the backbone for diffusion-based models and Stable Diffusion 3.5-Medium [8] for flow-based models. To ensure a fair comparison, we attempted to adapt the diffusion-based baselines to the flow-based backbone. However, similar to prior observations in [7, 11], directly converting diffusion-based baselines into flow-based counterparts consistently resulted in degraded performance despite stronger priors. Therefore, we report the results using their original backbones.

### B.1. FlowLPS Configuration

We employed a fixed number of Langevin-Proximal update steps,  $N_P = 15$  for our main experiments. A constant step size  $\zeta_t = 10^{-4}$  was used for Langevin dynamics across all timesteps. For the proximal optimization, we utilized the SGD optimizer. We used an initial learning rate of 0.5 for super-resolution and 0.1 for other tasks. To ensure stability during optimization, we applied a step-based learning rate decay schedule: for super-resolution, the learning rate is decayed by a factor of 0.85 every 5 iterations, and for inpainting, by 0.65 every 10 iterations. For the forward measurement operators, we adopted the implementations from DPS [4]. Based on empirical findings that negative prompts improve results, we used the negative prompt "blurry, noisy, a bad quality photo" for classifier-free guidance. All experiments were conducted with a Classifier-Free Guidance (CFG) scale of 2.0.

**Time Schedule.** Fig. 8 illustrates the Mean Squared Error (MSE) loss of the reconstructed clean image estimate  $\mathcal{D}(\mathbf{z}_{0|t}^*)$  as a function of timestep  $t$ , scaled relative to the maximum value. The results are averaged over 100 FFHQ images, for both super-resolution and deblurring tasks, with the deblurring curve representing the average of both Gaussian and motion deblurring tasks. We observed that the MSE decreases as  $t$  decreases, reaching a minimum around  $t \approx 0.2$  for deblurring and  $t \approx 0.3$  for super-resolution, before beginning to rise as  $t \rightarrow 0$ . Based on this trend, we adopted a truncated time schedule to stop the reverse process before significant divergence occurs. Specifically, we set the

sampling schedule start point to  $40 + \alpha$  (using the first 40 steps). We set  $\alpha = 5$  for super-resolution and  $\alpha = 3$  for other tasks, which align with the optimal stopping points observed in our analysis. We found these settings empirically provide the best trade-off between reconstruction fidelity (MSE) and perceptual details.

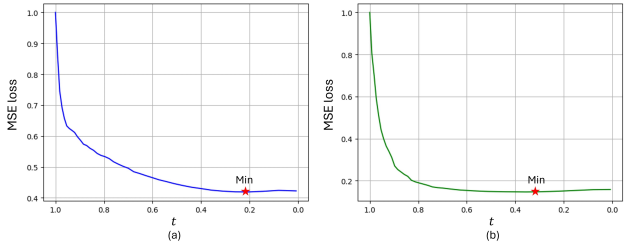


Figure 8. **Reconstruction MSE error vs. Timestep  $t$ .** (a) Deblurring, (b) Super-resolution. The plot shows the relative MSE of the estimated clean image  $\mathcal{D}(z_{0|t}^*)$  for deblurring (averaged over Gaussian/Motion) and super-resolution. The error minimizes around  $t \approx 0.2$  for deblurring and  $t \approx 0.3$  for super-resolution, justifying the use of task-specific truncated time schedules.

A detailed summary of hyperparameters for all tasks is provided in Table 3.

Table 3. **Hyperparameters for FlowLPS experiments.**  $N_L$  denotes the number of Langevin steps,  $N_P$  denotes the total number of Langevin-Proximal steps,  $\zeta_t$  denotes the step size of Langevin dynamics, and  $\alpha$  denotes the sampling schedule offset parameter.

	Inpainting (Box)	Inpainting (Random)	Gaussian Deblurring	Motion Deblurring	Super-resolution ( $\times 12$ )
$\zeta_t$	$1e-4$	$1e-4$	$1e-4$	$1e-4$	$1e-4$
$\alpha$	3	3	3	3	5
$N_L$	4	5	6	6	4
$N_P$	15	15	15	15	15

## B.2. Baselines Details

**DAPS** [27]. We configured the method with 5 ODE steps and 50 annealing scheduler steps, resulting in a total of 250 Number of Function Evaluations (NFEs). Optimal settings were determined via grid search on a validation set of 200 images. For instance, in the Gaussian deblurring task, we found the optimal setting to be 50 MCMC steps with a learning rate of  $10^{-6}$  and a CFG scale of 6.0. For super-resolution, we used 50 MCMC steps with a learning rate of  $10^{-5}$  with a CFG scale of 5.0.

**RLSD** [30]. Using 250 NFEs, we adopted the non-repulsive setting. Consistent with the original paper, we observed that the repulsive term reduced fidelity in our test cases. We set the CFG scale to 6.0 for all tasks.

**FlowDPS** [11]. We utilized 40 NFEs with 15 optimization steps per iteration and a CFG scale of 2.0. The step size

was set to 8.0 for super-resolution, Gaussian deblurring, and motion deblurring, and 12.0 for inpainting tasks.

**FlowChef** [17]. We used 40 NFEs with a single optimization step per iteration. Although we attempted to increase optimization steps to 15 for fairness, this did not yield performance gains. A step size of 1.5 was used across all tasks.

**FLAIR** [7]. Configured with 40 NFEs and 15 optimization steps per iteration. We used a CFG scale of 2.0 and followed default settings, except for super-resolution where the data term optimizer learning rate was set to 1.0.

**Flower** [20]. We used 40 NFEs, 15 optimization steps, and a CFG scale of 2.0. Consistent with the original author’s findings, the optional uncertainty term was found to destabilize restoration. Thus, we set  $\gamma = 0$ .

## C. Additional Ablation Studies

### C.1. Effectiveness of the Langevin-Proximal Update

While we demonstrated the quantitative trade-off of Langevin steps in Section 4.3 of the main paper, here we provide additional visual evidence to further clarify the impact of  $N_L$ . Fig. 9 compares the visual quality across different  $N_L$  settings:  $N_L = 0$  (pure optimization) leads to high FID/LPIPS due to blurriness. Moderate stochasticity ( $N_L = 5 - 7$ ) achieves an optimal balance, producing detailed restorations while maintaining measurement consistency. Conversely, excessive Langevin steps ( $N_L > 10$ ) degrade perceptual quality, introducing high-frequency artifacts and grainy noise patterns. Fig. 9 visualizes these extremes, contrasting the over-smoothed textures of pure optimization ( $N_L = 0$ ) with the noisy artifacts of excessive Langevin dynamics ( $N_L = 15$ ).

### C.2. Detailed Analysis of pCN Steps

Recall the pCN transition kernel defined in Eq. (11). Assuming the target distribution is the standard Gaussian  $\mathcal{N}(0, I)$ , the acceptance probability is:

$$\begin{aligned} & \min \left\{ 1, \frac{p_{\text{tar}}(\hat{x}_{\text{new}})q_{\text{prop}}(\hat{x}_{\text{old}}|\hat{x}_{\text{new}})}{p_{\text{tar}}(\hat{x}_{\text{old}})q_{\text{prop}}(\hat{x}_{\text{new}}|\hat{x}_{\text{old}})} \right\} \\ &= \min \left\{ 1, \frac{\mathcal{N}(\hat{x}_{\text{new}}; 0, I)\mathcal{N}(\hat{x}_{\text{old}}; \rho_t \hat{x}_{\text{new}}, (1 - \rho_t^2)I)}{\mathcal{N}(\hat{x}_{\text{old}}; 0, I)\mathcal{N}(\hat{x}_{\text{new}}; \rho_t \hat{x}_{\text{old}}, (1 - \rho_t^2)I)} \right\} \\ &= \min\{1, 1\} = 1. \end{aligned} \quad (17)$$

This confirms that every proposed step is accepted. Table 4 compares performance across varying pCN steps. We observed that increasing the number of pCN steps tends to improve PSNR slightly but degrades perceptual metrics. As visualized in Fig. 10, multiple pCN steps dilute the structural information embedded in the predicted noise  $\hat{x}_{1|t}^{(0)}$ , leading to progressive over-smoothing. Hypothesizing that stronger stochastic exploration is beneficial primarily in the early stages, we further experimented with a linear decay schedule

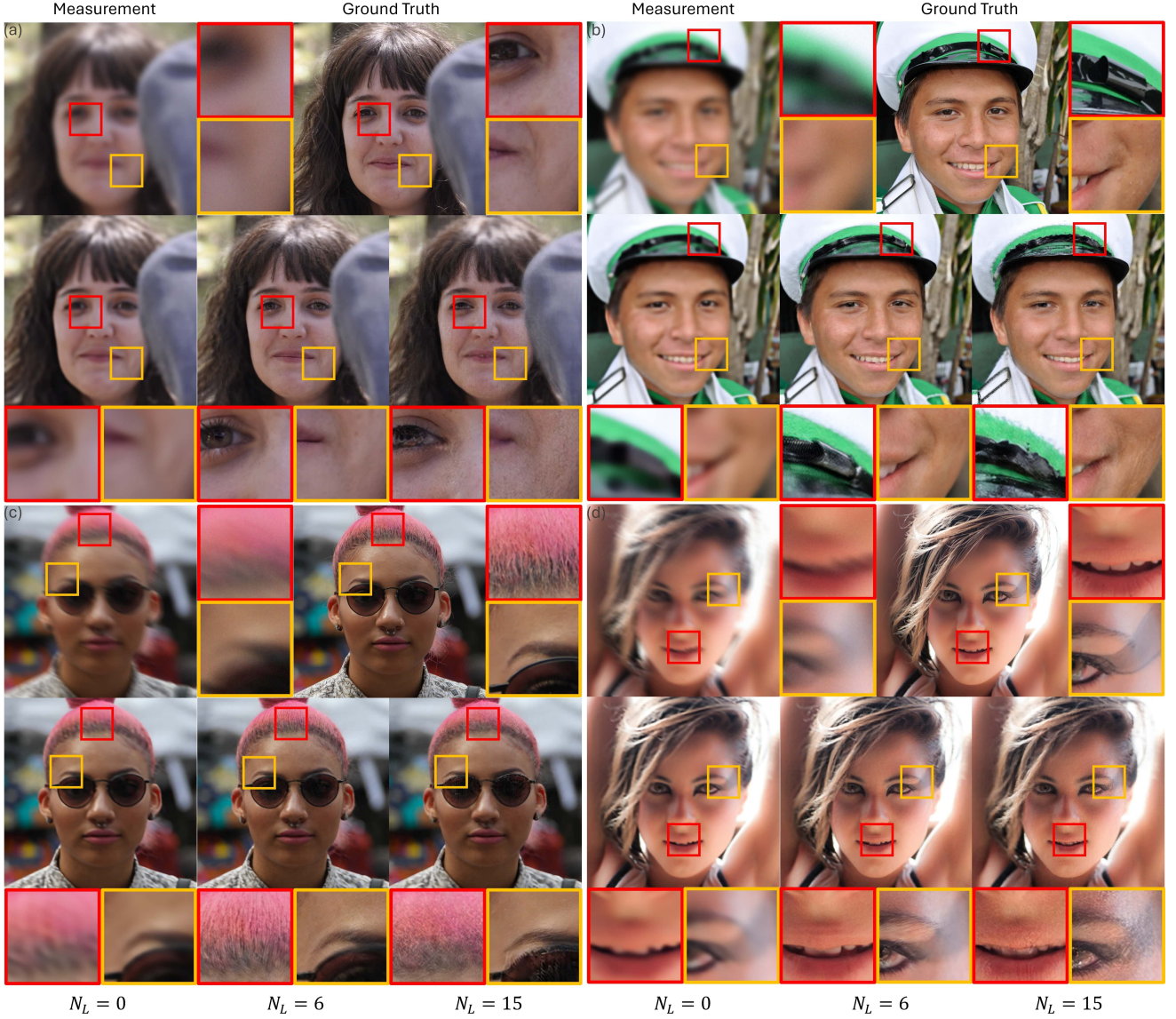


Figure 9. **Visual artifacts from excessive Langevin steps.** (a), (b) Gaussian deblurring, (c), (d) Motion deblurring.  $N_L = 0$  yields over-smoothed results.  $N_L = 15$  introduces speckled, high-frequency noise.  $N_L = 6$  produces clean, high-fidelity images.

for pCN steps ( $4 \rightarrow 1$ ). This strategy aims to balance early-stage exploration with late-stage exploitation. As shown in Table 4, this decay strategy effectively improves FID scores, surpassing the 1-step baseline in generation-heavy tasks such as Box Inpainting and Super-Resolution. This supports our hypothesis that early noise exploration aids in generating realistic textures. However, this perceptual improvement comes at the cost of the pixel-level fidelity (PSNR) gains observed in fixed multi-step settings. Furthermore, in deblurring tasks, the decay strategy offers only marginal benefits over the single-step baseline. Therefore, considering the trade-off between computational efficiency, consistent performance across diverse tasks, and implementation sim-

plicity, we conclude that a single pCN step is the most robust choice.

### C.3. Dynamic Computational Budget Allocation

We provide the detailed metrics for the dynamic budget allocation strategy discussed in the main paper. In Section 4.3.3, we hypothesized that the necessity of Langevin steps  $N_L$  diminishes over time. In the early sampling stages (high  $t$ ), the estimate is far from the mode, requiring robust Langevin exploration. In later stages (low  $t$ ), the Tweedie estimate from the flow model already lies close to the posterior mode, rendering intensive Langevin steps redundant.

To test this, we implemented a linear decay schedule

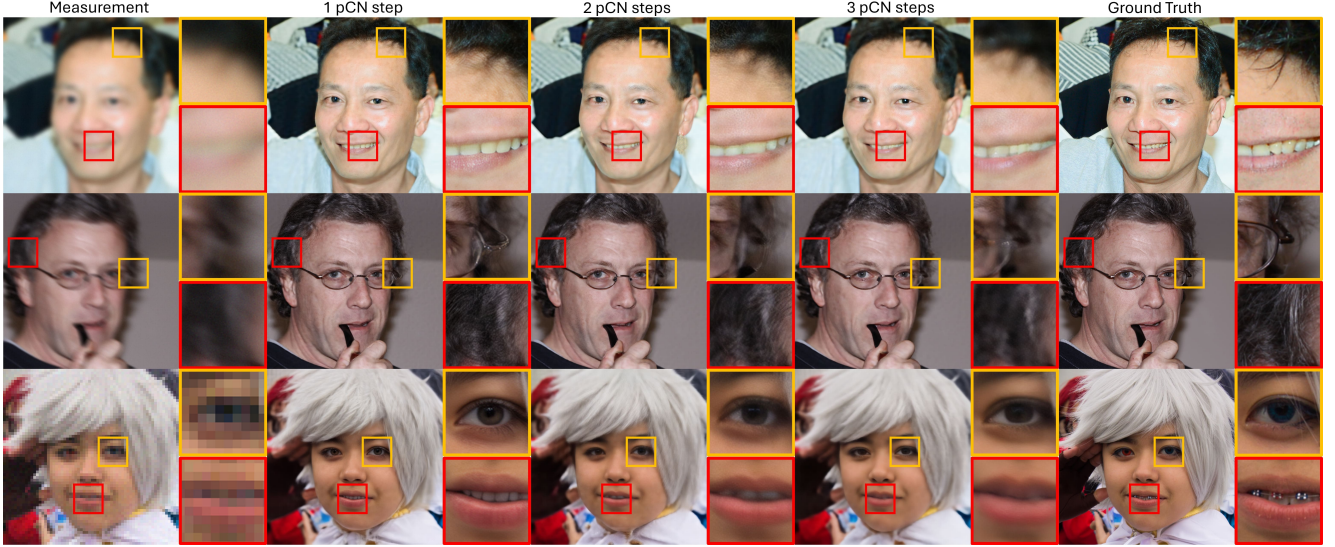


Figure 10. **Effect of multiple pCN steps.** Increasing pCN steps leads to progressive over-smoothing.

Table 4. **Ablation on the number of pCN re-noising steps (FFHQ 0.2k).** "Decay (4 → 1)" indicates a linear reduction of pCN steps from 4 to 1 over the sampling process. While the decay strategy offers the best FID for inpainting and super-resolution, the single-step approach provides the best overall balance.

Task	# pCN	PSNR (↑)	SSIM (↑)	FID (↓)	LPIPS (↓)
Inpainting (Box)	1	21.94	<b>0.846</b>	42.15	<b>0.106</b>
	2	21.67	0.842	42.55	0.110
	3	<b>21.98</b>	<b>0.846</b>	43.87	0.108
	Decay (4 → 1)	21.46	0.843	<b>40.34</b>	0.110
Gaussian Deblurring	1	27.83	0.744	<b>53.83</b>	<b>0.126</b>
	2	27.97	0.750	54.62	0.129
	3	<b>28.01</b>	<b>0.752</b>	56.36	0.129
	Decay (4 → 1)	27.75	0.745	54.32	0.128
Motion Deblurring	1	29.86	0.780	<b>35.97</b>	<b>0.065</b>
	2	30.10	0.789	37.09	0.067
	3	<b>30.13</b>	<b>0.790</b>	37.60	0.067
	Decay (4 → 1)	30.02	0.786	36.90	0.067
Super-Resolution (×12)	1	27.12	0.720	62.44	<b>0.154</b>
	2	<b>27.14</b>	<b>0.725</b>	65.04	0.158
	3	<b>27.14</b>	<b>0.725</b>	65.46	0.161
	Decay (4 → 1)	26.92	0.715	<b>62.03</b>	0.156

for  $N_L$ , effectively reducing it to zero towards the end of sampling. Our target was to reduce the total computational budget to  $N_P = 10$  in the final sampling block. For deblurring, reducing  $N_L$  from 6 → 1 naturally aligned with this target ( $N_P = 10$ ). However, for super-resolution and inpainting, reducing  $N_L$  from 4 → 0 resulted in  $N_P = 11$  steps. Thus, to strictly match the target budget of  $N_P = 10$ , we additionally removed one proximal optimization step for these tasks. As shown in Table 5, this dynamic allocation maintains performance parity with the fixed schedule. This validates our hypothesis: Langevin dynamics are crucial for early-stage anchoring but can be safely reduced in later stages to save computational cost without sacrificing quality.

Table 5. **Performance comparison: Fixed vs. Decaying  $N_L$ .** "Decay" indicates a linear reduction of Langevin steps over iterations, adjusted to meet a reduced computational budget ( $N_P = 10$ ) in the final sampling block. The results show that tapering off exploration in later stages maintains performance.

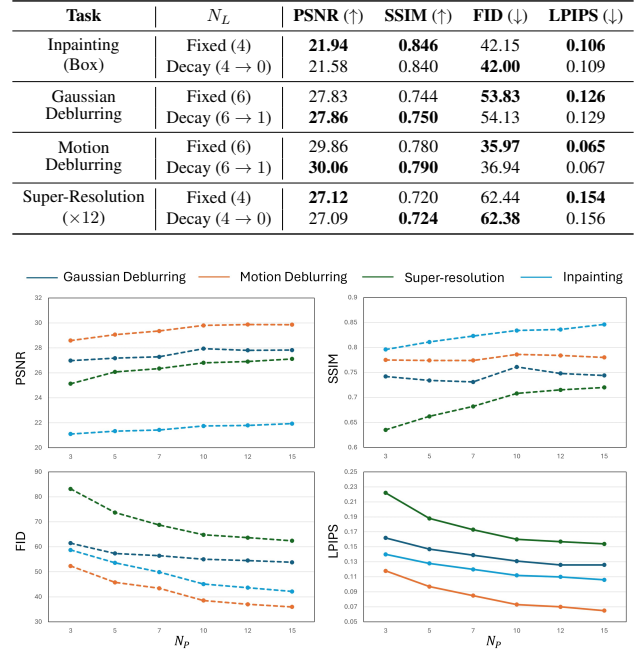


Figure 11. **Performance vs. Proximal Steps ( $N_P$ ).** Performance gains show diminishing returns beyond  $N_P \approx 10$ , suggesting that  $N_P = 15$  serves as a robust operating point for maximum quality, while lower  $N_P$  remains viable for efficiency.

Separately, we also investigated the trade-off between performance and the total computational budget determined by the number of Langevin-Proximal steps  $N_P$ . Fig. 11 indicates that performance gains show diminishing returns beyond  $N_P \approx 10$ . While we utilized a fixed  $N_P = 15$  in our main experiments to prioritize maximum quality, these results suggest that a lower fixed  $N_P$  (e.g.,  $N_P = 10$ ) remains a viable choice for time-constrained applications.

Finally, to quantify the practical efficiency gains derived from both strategies, we measured the inference time on the inpainting task using a NVIDIA RTX 3090 GPU. We evaluated two VAE backbones: the standard "Large VAE" from Stable Diffusion 3 and the distilled "Tiny VAE", which is also adopted by FLAIR [7] for faster decoding. Table 6 summarizes the results. The column "15 → 10" represents the  $N_L$  decay strategy. As shown, the decay strategy reduces inference time compared to the fixed  $N_P = 15$  setting (e.g., 262.2s → 232.7s with Large VAE) while preserving reconstruction quality. Furthermore, utilizing the Tiny VAE significantly accelerates the process (down to  $\approx 30$ s), making FlowLPS highly practical for real-time applications.

To quantify the efficiency gains, we measured the inference time on the inpainting task using a RTX 3090 GPU. We evaluated two VAE backbones: the standard "Large VAE" from Stable Diffusion 3 and the distilled "Tiny VAE", which is also adopted by FLAIR [7] for faster decoding. Table 6 summarizes the results. The column "15 → 10" represents the  $N_L$  decay strategy described above. As shown, the decay strategy reduces inference time compared to the fixed  $N_P = 15$  setting while preserving reconstruction quality. Furthermore, utilizing the Tiny VAE significantly accelerates the process, making FlowLPS highly practical for real-time applications.

**Table 6. Runtime analysis on inpainting task.** We compare the inference time (seconds per image) across different proximal budgets ( $N_P$ ). "15 → 10" denotes the dynamic decay strategy where  $N_L$  is linearly reduced. "Large VAE" refers to the standard Stable Diffusion VAE, while "Tiny VAE" refers to the distilled efficient decoder used in FLAIR.

$N_P$	3	5	7	10	12	15 → 10	15
large VAE	66.13	101.1	161.6	183.8	217.8	232.7	262.2
tiny VAE	15.63	18.48	21.79	24.74	27.70	29.34	31.65

## D. Additional Qualitative Results

### D.1. Visual Analysis of Generative Bias in FLAIR

As discussed in the main paper (Sec. 4.2), FLAIR tends to prioritize perceptual quality over fidelity, often leading to hallucinations. Fig. 12 presents a detailed visual comparison. While FLAIR generates sharp images, it often alters semantic attributes such as facial expressions or specific features

(e.g., eye shape, wrinkles). This suggests that the method relies heavily on its generative prior rather than the measurement, resulting in plausible but unfaithful reconstructions. In contrast, FlowLPS faithfully recovers the ground truth identity.

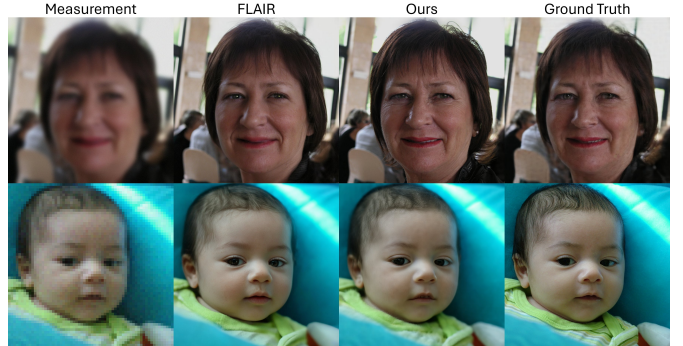


**Figure 12. Visual evidence of generative bias in FLAIR.** Top: Gaussian Deblurring, Bottom: Super-Resolution. While FLAIR generates sharp images, it ignores the measurement's underlying structure in favor of its generative prior. Note how FLAIR alters facial features (e.g., eye shape), prioritizing the generation of "plausible" faces over the recovery of the true identity. In contrast, FlowLPS faithfully recovers the semantic attributes of the Ground Truth.

## D.2. Full Reconstruction Results

We provide additional qualitative comparisons on FFHQ and DIV2K for all tasks. Note that FlowLPS consistently recovers sharper textures and more semantically plausible structures compared to baselines across all tasks.

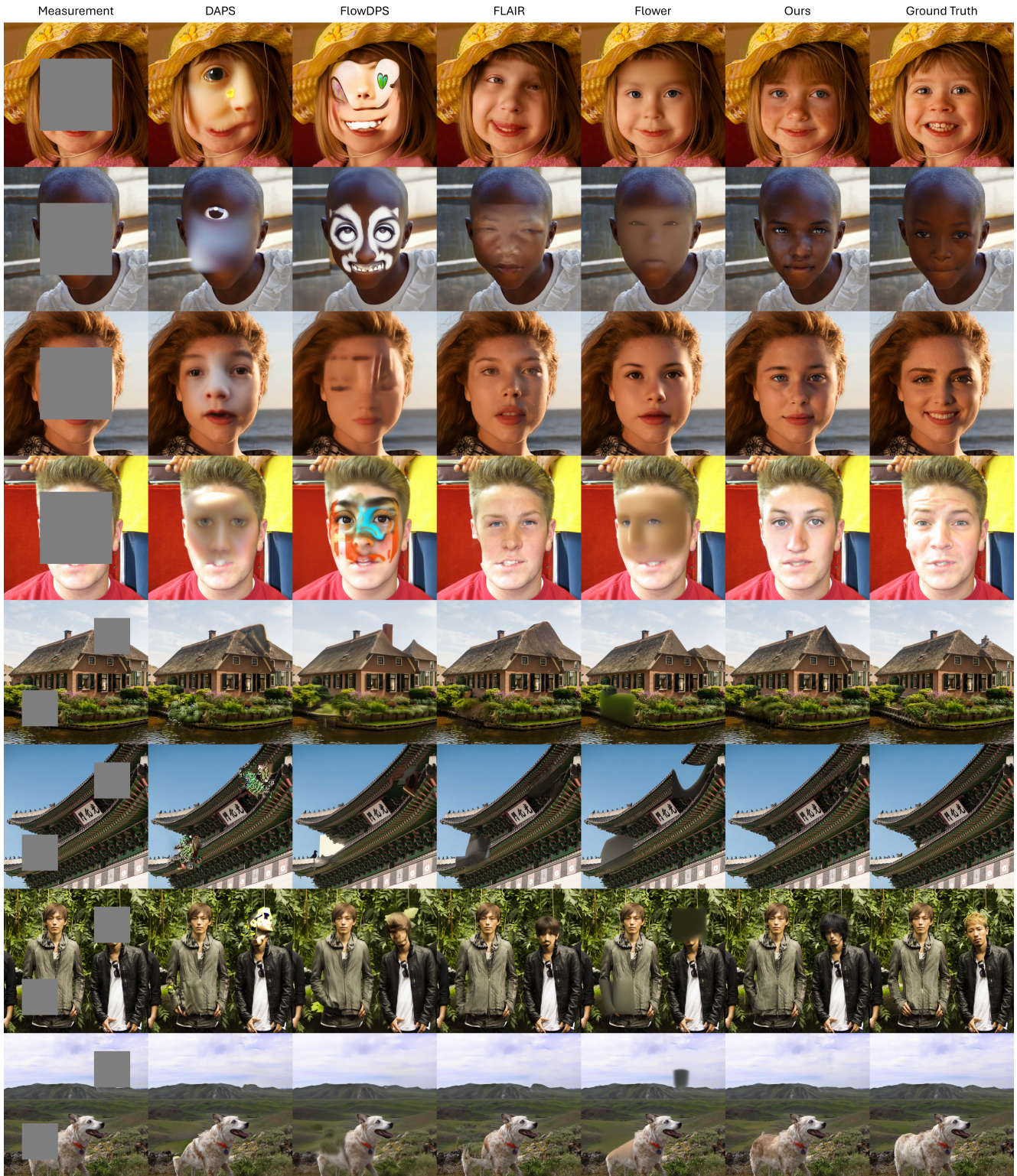


Figure 13. Box Inpainting results on FFHQ and DIV2K.

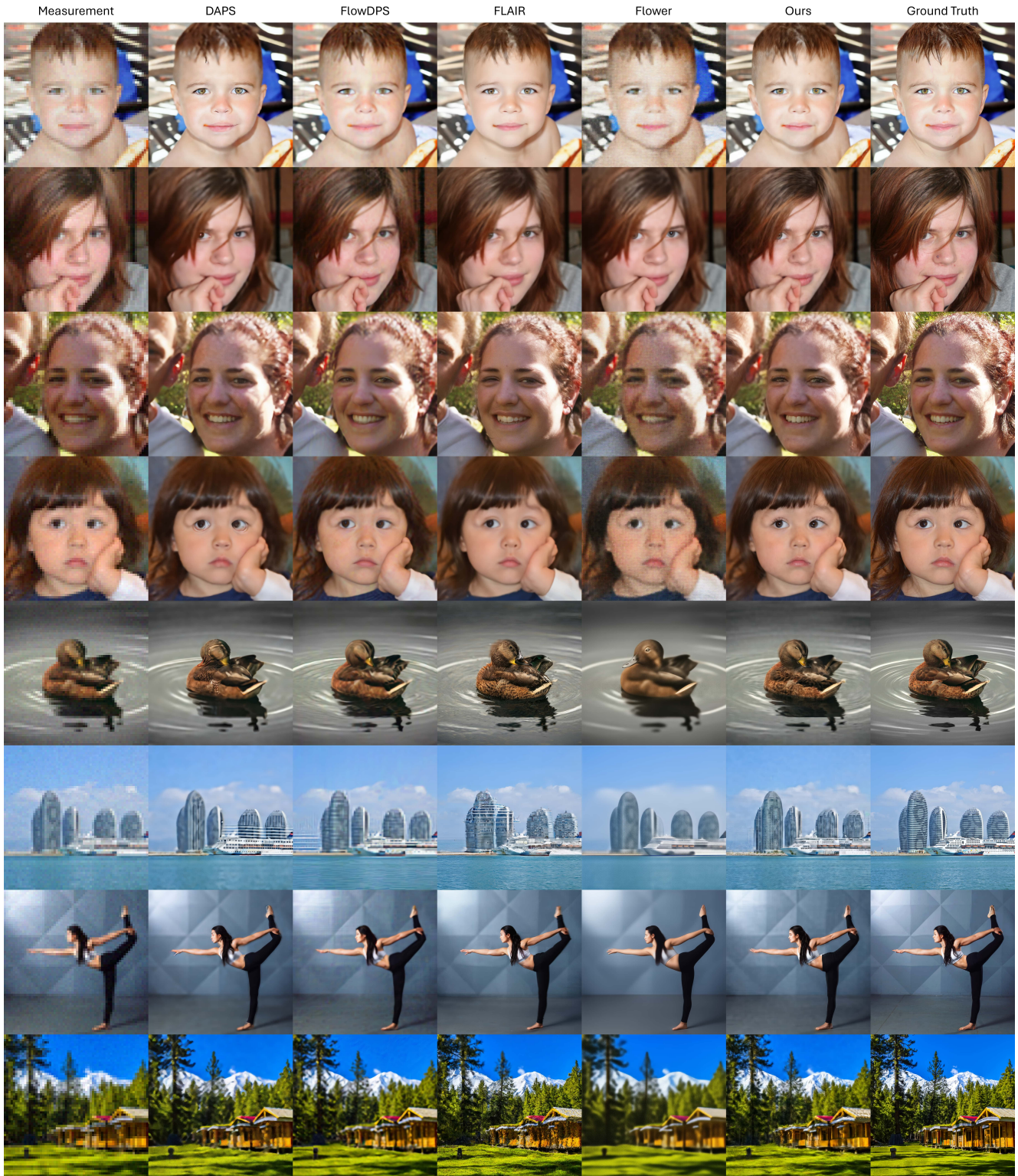


Figure 14. Super-Resolution( $\times 12$ ) results on FFHQ and DIV2K.

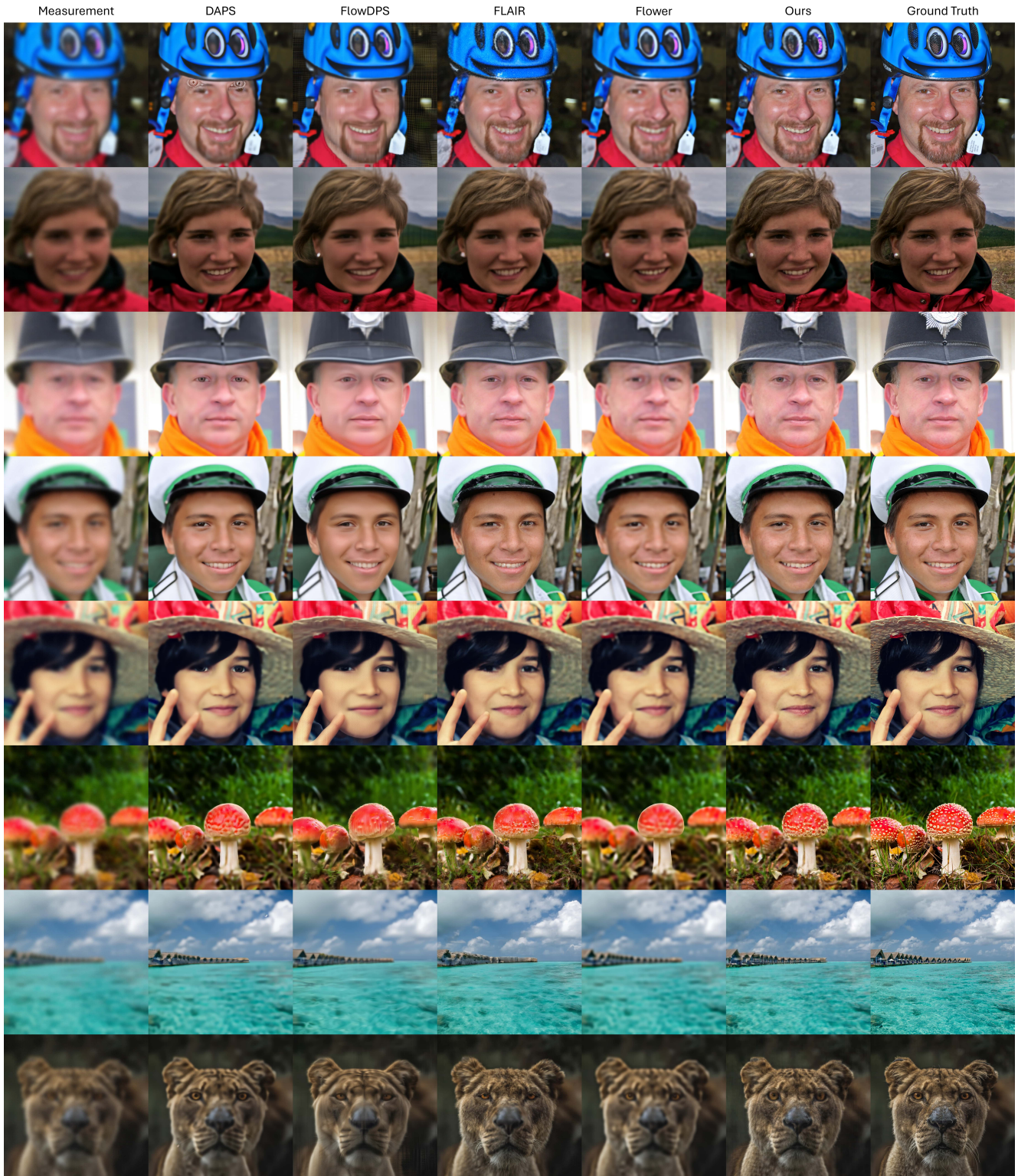


Figure 15. Gaussian deblurring results on FFHQ and DIV2K.

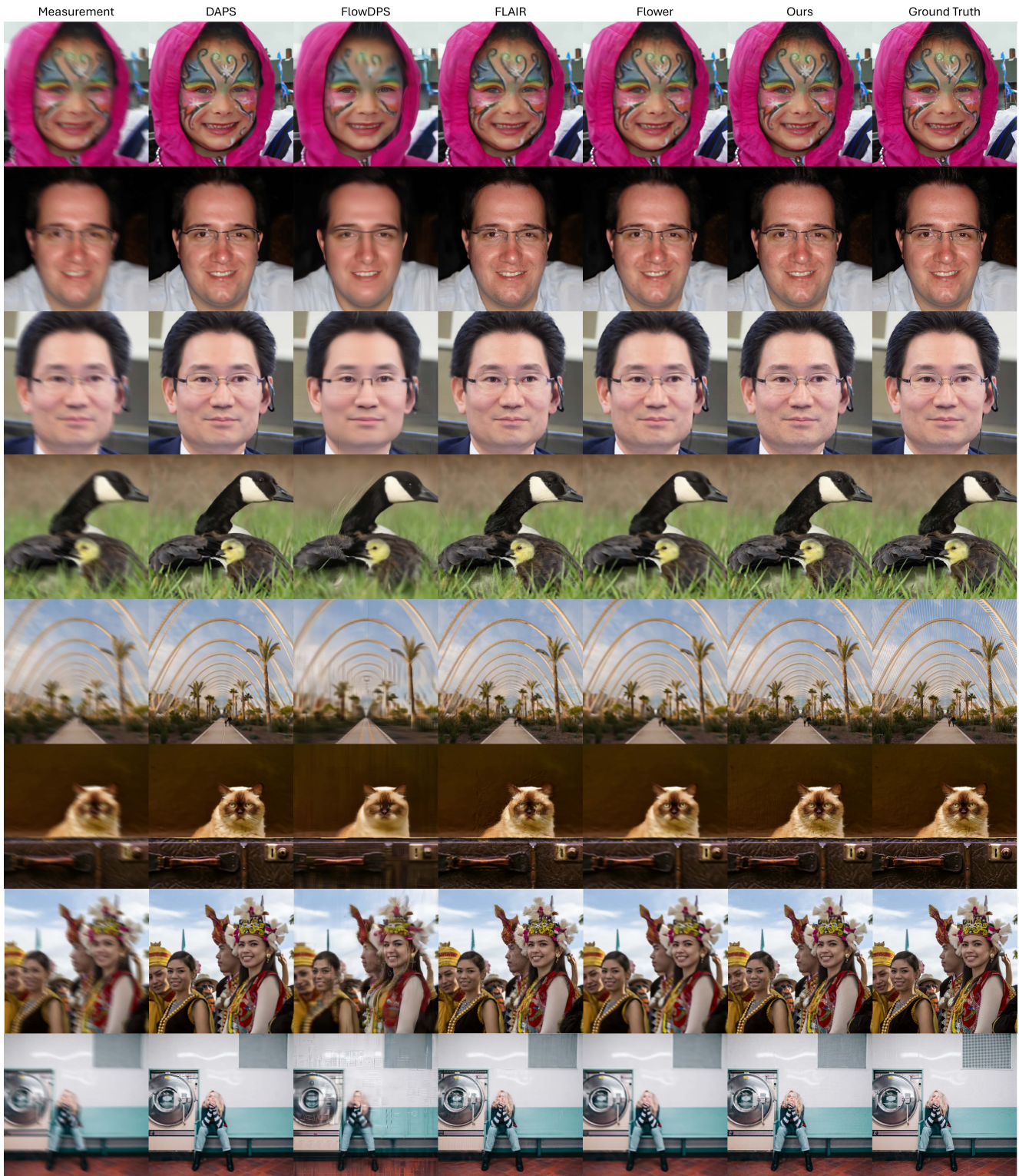


Figure 16. Motion deblurring results on FFHQ and DIV2K.

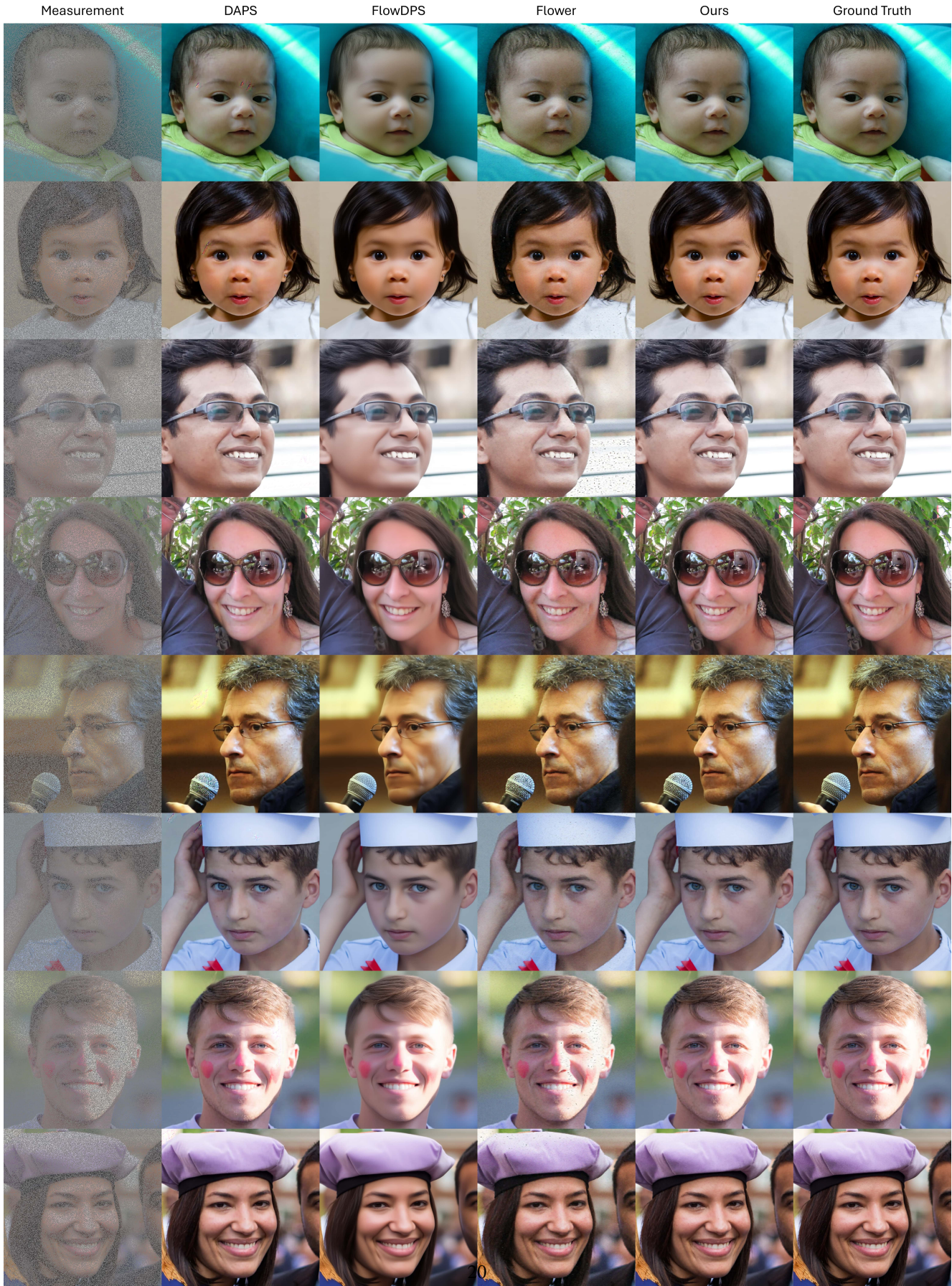


Figure 17. Random Inpainting results on FFHQ and DIV2K.